Astronomy & Astrophysics manuscript no. M33clusts˙grossi
August 8, 2011

© ESO 2011

arXiv:1006.1281v2 [astro-ph.CO] 5 Aug 2011

Young stellar clusters and associations in M33

M. Grossi[1,2], E. Corbelli[2], C. Giovanardi[2], and L. Magrini[2]

[1] CAAUL, Observatório Astronómico de Lisboa, Universidade de Lisboa, Tapada de Ajuda, 1349-018, Lisboa, PT
e-mail: `grossi@oal.ul.pt`

[2] INAF-Osservatorio Astrofisico di Arcetri, L.go E. Fermi 5, 50125 Firenze, IT

ABSTRACT

Aims. We analyse multi-wavelength observations of 32 young star clusters and associations in M33 with known oxygen abundance ($8 < 12 + \log(O/H) < 8.7$). The data set includes ultraviolet (UV), optical, mid-infrared (MIR), CO (1-0) and 21-cm line (HI) observations. We derive the spectral energy distribution (SED) of these systems and the properties of their gaseous environment to investigate the process of star formation and the interplay with the interstellar medium (ISM).
Methods. We determine age, bolometric luminosities, masses, and the extinction by comparing the multi-band integrated photometry to single-age stellar population models. The best-fit solutions have been obtained using the Large Magellanic Cloud (LMC) extinction curves.
Results. The stellar system ages range between 2 and 15 Myr, masses are between 3×10^2 and 4×10^4 $M_\odot$, and the intrinsic extinction, A_V, varies from 0.3 to 1 mag. We find a correlation between age and extinction (young clusters being more reddened than older ones), and between the cluster mass and size. From the MIR emission we infer the presence of a dust component around the clusters whose fractional luminosity at 24 μm, L_{24}/L_{Bol}, decreases with the galactocentric distance. However, the total infrared luminosity inferred from L_{24} is smaller than what we derive from the extinction corrections. We also find that the Hα luminosity predicted by population synthesis models is higher than the observed one, especially for low-mass systems ($M < 10^4$ $M_\odot$). This difference is reduced, but not erased, when the incomplete sampling of the initial mass function (IMF) at the high-mass end is taken into account.
Conclusions. Our results suggest that a non-negligible fraction of UV ionising and non-ionising radiation is leaking into the ISM outside the HII regions. This agrees with the large UV and Hα diffuse fractions observed in M33, but it implies that stellar systems younger than 3 Myr retain, on average, only 30% of their Lyman-continuum photons. However, the uncertainties in cluster ages and the stochastic fluctuations of the IMF do not allow us to accurately quantify this issue. We also consider the possibility that this discrepancy is the consequence of a suppressed or delayed formation of the most massive stars, given that it mainly affects the young and less massive clusters. We do not find any clear correlation between the cluster mass and the gas surface density or metallicity.

Key words. Galaxies: individuals(M33) – Stars: formation – Galaxies:star clusters – Galaxies:ISM

1. Introduction

M33 is the nearest late-type spiral, its properties being in between earlier-type spirals like the Milky Way and M31 and the star-forming dwarf galaxies in the Local Group. With a relatively high star-formation rate per unit area (3.4×10^{-3} $M_\odot$ yr^{-1} kpc^{-2}), seven times higher than M31 (Kennicutt 1998) and a low inclination, M33 is an ideal environment to study the properties of young stellar systems and star-forming regions.

Young star clusters and associations are important for studying the ongoing star-formation activity and the chemical evolution of their parent galaxy. The study of young stellar populations enables us to analyse the initial phase of the cluster evolution, which is mainly driven by hot massive stars. Despite their short lifetime, these stars play an important role in galaxy evolution, because they are the main source of ionisation, heating, and the chemical enrichment of the interstellar medium (ISM). Massive stars trace the current star-formation activity, they power the infrared (IR) radiation of dust and, at the end of their lives, they eventually trigger further star-formation events via supernova explosions. Moreover, from the properties of the gas and dust distribution of the cluster environment one can better understand the mutual relation between star formation and the ISM.

A number of studies have analysed the cluster population of M33 both from space (Chandar et al. 1999, 2001) and from the ground (Ma et al. 2001, 2002, 2004), although they have mainly concentrated on rather evolved stellar systems with ages between a few tens of Myr and few Gyrs. Nonetheless, the population of young stellar systems ($\lesssim$ 10 Myr) in M33 has not been thoroughly investigated, and only a few studies have been dedicated to such young star-forming systems.

A recent multi-wavelength analysis of radio-selected sources in M33 led to the identification of 11 young, optically-visible stellar clusters without finding any highly obscured systems (Buckalew et al. 2006). Extinction seems generally lower in M33 than in the Milky Way, and the absence of large molecular complexes (Rosolowsky et al. 2007) may imply that even in an early star-formation phase stellar clusters may not be highly extincted. Corbelli et al. (2009) examined the properties of young stellar clusters in M33 selected at 24 μm with Hα counterparts and stressed the importance of combining multiple wavelength observations (from the UV to MIR) to study star-forming sites and to improve the understanding of massive star formation. Verley et al. (2007, 2009) showed that MIR images of M33 obtained with the *Spitzer* telescope allow us to identify HII regions with 24 μm luminosities as low as 2×10^{37} erg s^{-1} and to study the star-formation properties of the M33 disc.

Here we present a multi-wavelength analysis of a sample of 32 young clusters and associations in M33 selected from the catalogues of emission-line objects of Magrini et al. (2007b) and Rosolowsky & Simon (2008). Our aim was to define a list of young stellar systems selected on the basis of their Hα emission, for which a measure of their metal abundance was available. In addition, our objects have a 24 μm counterpart in the catalogue of Verley et al. (2007). The final sample includes well known giant H ii regions such as NGC588 and IC132, located in the outskirts of the galaxy, large OB associations such as C400 and B0222, and more compact H ii regions such as B0670 or LGCHII11 with sizes smaller than 10 pc.

We use UV (GALEX), *UBVRI* (Local Group Survey), MIR (*Spitzer* IRAC and MIPS) observations to constrain ages, masses, extinction, and dust properties of the sample from the comparison to model spectral energy distributions (SEDs). We search for possible correlations among the derived parameters, we compare the properties of these stellar systems to their metallicity, we look for radial gradients in the observed emissions at different wavelenghts, and finally, we use archival CO and H i observations to relate the total stellar masses to the local gas content.

The data are presented in Sect. 2, and in Sect. 3 we discuss the sample selection. The method to derive the photometric measurements in the different bands is described in Sect. 4, while an overview of the SED-fitting technique is given in Sect. 5. The results are discussed topic by topic in Sect. 6. The issue of the ionising photon deficiency within the clusters is analysed in Sect. 7. The properties of the gaseous environment of the sample are presented in Sect. 8, and in Sect. 9 we summarise our results and conclusions.

2. The data set: archival UV, optical and IR images

2.1. Galex images

We used Galaxy Evolution Explorer (GALEX; Martin et al. 2005) observations of M33 in the far-UV (FUV, λ_{eff} = 1528 Å) and near-UV (NUV, λ_{eff} = 2271 Å), distributed by Gil de Paz et al. (2007). The angular resolution (FWHM) is $\sim 4''$ in the FUV and $\sim 5''.5$ in the NUV images, corresponding to approximately 20 pc at the M33 distance. The exposure time was 3400 sec in both filters. A more detailed description of GALEX observations of M33 and of the data reduction and calibration procedures can be found in Thilker et al. (2005).

2.2. Ground-based optical data: the Local Group Survey

UBVRI images of M33 have been taken from the Local Group Survey (LGS) of galaxies currently forming stars (Massey et al. 2006). M33 observations have been performed with the Kitt Peak National Observatory 4-m telescope using the wide-field Mosaic cameras. Narrowband images through the filters centred on [O iii] λ5007, Hα and [S ii] λ6731 are also provided (Massey et al. 2007). The data are resampled to a scale of 0.27 arcsec/pixel. The FWHM of the point spread function in the *V* band is $1''.1$, corresponding to ∼4 pc. More details about the observations and data reduction can be found in these papers.

We also made use of an optical narrowband Hα image of M33 obtained with the 0.6 meter Burrell-Schmidt telescope at Kitt Peak National Observatory (Hoopes & Walterbos 2000). The 2048 × 2048 pixel CCD provides a field of view of 1.15 × 1.15 square degrees, with a scale of 2.03 arcsec/pixel. The final mosaic covers an area of about 1.75 × 1.75 square degrees. More details on the observations and reduction procedure can be found in Hoopes & Walterbos (2000).

Table 1. Sample of young clusters in M33 selected in this work.

ID	Name	RA	DEC	12 + log(O/H)
		J2000.0		
1	B691	01:34:16.6	30:51:54	8.26 ± 0.02 ^{a}
2	VGHC 2-84	01:34:06.7	30:48:56	8.35 ± 0.04 ^{a}
3	IC132	01:33:15.8	30:56:45	8.08 ± 0.04 ^{a}
4	B290	01:33:11.4	30:45:15	8.21 ± 0.06 ^{a}
5	NGC588	01:32:45.9	30:38:54	8.31 ± 0.06 ^{a}
6	C400	01:32:44.4	30:35:17	7.98 ± 0.08 ^{b}
7	MA2	01:34:15.6	30:37:11	8.33 ± 0.08 ^{a}
8	S14	01:34:13.7	30:33:45	8.30 ± 0.11 ^{b}
9	GDK99 128	01:33:59.9	30:32:44	8.47 ± 0.06 ^{a}
10	C129a	01:33:23.4	30:31:35	8.45 ± 0.08 ^{b}
11	C121	01:33:17.1	30:31:11	8.35 ± 0.06 ^{b}
12	B0221	01:33:09.8	30:27:23	8.28 ± 0.10 ^{b}
13	B0222	01:33:25.0	30:25:31	8.10 ± 0.18 ^{b}
14	C022	01:33:01.6	30:24:31	8.31 ± 0.08 ^{b}
15	B0745	01:34:37.6	30:34:55	8.07 ± 0.10 ^{a}
16	B0670	01:34:03.3	30:53:09	8.28 ± 0.07 ^{a}
17	B0637	01:33:50.6	30:56:33	8.34 ± 0.05 ^{a}
18	LGC HII 3	01:32:45.9	30:41:35	8.24 ± 0.05 ^{a}
19	B0706	01:34:42.2	30:31:42	8.32 ± 0.12 ^{a}
20	LGC HII 11	01:34:42.2	30:24:00	8.17 ± 0.06 ^{a}
21	B0261	01:32:54.6	30:23:22	8.36 ± 0.08 ^{b}
22	MCM00Em24	01:33:10.8	30:18:08	8.18 ± 0.25 ^{a}
23	B0254	01:33:21.2	30:17:58	8.16 ± 0.19 ^{b}
24	LGC HII 2	01:32:43.0	30:19:31	8.25 ± 0.06 ^{a}
25	B0045	01:33:29.0	30:40:24	8.49 ± 0.04 ^{a}
26	B0029	01:33:47.8	30:38:38	8.21 ± 0.10 ^{b}
27	B0016	01:33:50.1	30:37:30	7.98 ± 0.19 ^{b}
28	B0033b	01:33:34.9	30:37:05	8.40 ± 0.08 ^{b}
29	B0015b	01:33:50.3	30:33:42	8.73 ± 0.23 ^{b}
30	B0013c	01:33:54.1	30:33:10	8.26 ± 0.12 ^{b}
31	B0208f	01:33:34.1	30:32:13	8.07 ± 0.06 ^{b}
32	C403	01:33:07.6	30:31:01	8.27 ± 0.07 ^{b}

Notes. The identification names are from: B–Boulesteix et al. (1974); C– Courtes et al. (1987); GDK99–Gordon et al. (1999); LGC-HII-n–Magrini et al. (2007b); VGVC–Viallefond et al. (1986); MCM00–Magrini et al. (2000); MA–Mayall & Aller (1942); S–Searle (1971). Substructure designations within individual cluster (indicated by the letters at the end of their name) are taken from Hodge et al. (2002). The oxygen abundance determinations are from: $^{(a)}$ Magrini et al. (2007b); $^{(b)}$ Rosolowsky & Simon (2008)

2.3. Spitzer images

Spitzer IRAC and MIPS images of M33 were obtained under the Guaranteed Time Observer (GTO) programme PID 5 (PI R. Gehrz). We used the IRAC (3.6-8 μm) and MIPS (24 μm) maps of M33 produced by Verley et al. (2007). The spatial resolution of the IRAC maps is between $1''.7$ and $2''$(∼ 7 pc), while at 24 μm it is $6''$(24 pc). The map scale is 1.2 arcsec/pixel in both IRAC and MIPS images.

2.4. CO and HI maps

We used the 3-mm CO map of M33 (J=1-0 rotational line) obtained from the combination of the Berkeley Illinois

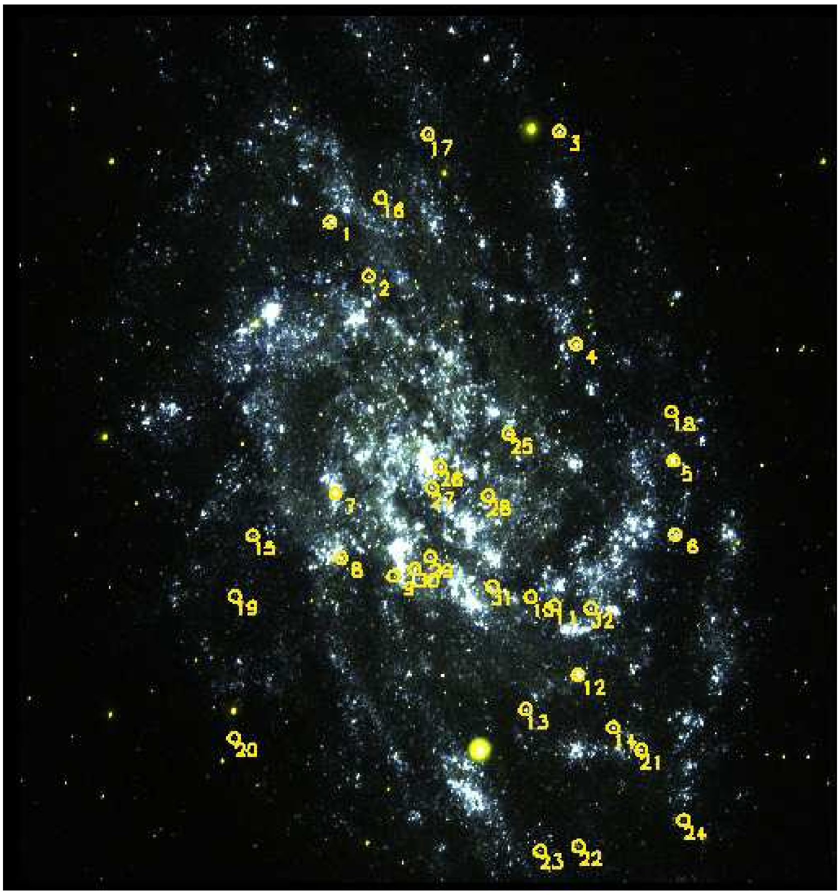

Fig. 1. Location of the 32 clusters selected in this study, overlayed on the GALEX (FUV and NUV) images of M33.

Maryland Association (BIMA) array (Engargiola et al. 2003; Rosolowsky et al. 2007) and the Five College Radio Astronomy Observatory (FCRAO) single dish (Heyer et al. 2004). The final resolution of the merged map is 13″. The median noise level of the channel maps is 240 mK, corresponding to a mass sensitivity of 5 $\times 10^4$ $M_\odot$ (4σ detection in two adjacent channels; see Rosolowsky et al. 2007) using a conversion factor X = 2 $\times 10^{20}$ $\mathrm{cm^{-2}}$ $\mathrm{(K\ km\ s^{-1})^{-1}}$.

The 21-cm observations of M33 have been taken at the Westerbork Radio Synthesis Telescope (WRST) array (Deul & van der Hulst 1987), with a spatial resolution of 24″× 48″.

3. Sample selection

The sample was selected from the catalogues of emission line objects of Magrini et al. (2007b) and of Rosolowsky & Simon (2008). The two catalogues contains 72 and 61 HII regions respectively. The oxygen abundances were obtained using the temperature-sensitive emission line [OIII] λ4363, with a direct measurement of the electron temperature. The condition of a measured and not assumed electron temperature is essential, because the determination of the ionic and total chemical abundances exponentially dependends on it.

The 32 HII regions of the sample were selected on the basis of their shape and their position, preferentially round and/or located in regions of the galaxy not too crowded in the Hα map. Then we searched for a 24 μm counterpart in the *Spitzer*/MIPS map of Verley et al. (2007), and by cross-correlating the two lists of objects we ended up with 25 sources with metal abundances within the range $8 < 12 + \log(\mathrm{O/H}) < 8.7$. We then added seven more regions at large galactocentric radii, which have a clear detection in the 24 μm map even though they are not included in the Verley et al. (2007) catalogue. The final sample includes well known giant HII regions such as NGC588 and IC132, which are located in the outskirts of the galaxy, large OB association as C400 and B0222, and more compact HII regions such as B0670 or LGCHII11 with sizes smaller than 10 pc. Figure 1 shows the position of the selected clusters and associations overlayed on the GALEX (FUV) image. In the rest of the paper we will refer to these young stellar systems by using the term "clusters" even though, in many cases, their size is larger than that of typical bound clusters.

4. Multi-wavelength photometry

We performed aperture photometry within circular regions choosing different apertures for each object. The aperture radius was defined on the basis of the extent of the *V* radial profiles, given the better resolution of the LGS images. The same position and aperture radius was applied to extract the photometry in the different bandpasses. The measurements were obtained using the IDL routine APER. Background subtraction was not straightforward because the clusters are found in different local environments. The contamination of nearby bright stars depends mainly on the object location in the galaxy and on the age of the background stellar population, and this is particulary critical in the *R*, *I* bands where the contamination by older stars is higher. The annuli for the background determination were selected indi-

Table 2. UV and optical photometric measurements. The last column displays the aperture radius used for the photometry.

ID	FUV AB mag	NUV AB mag	U AB mag	B AB mag	V AB mag	R AB mag	I AB mag	r_{ap} ($''$)
01	15.22±0.00	15.31±0.00	14.80±0.08	14.63±0.06	14.66±0.04	14.76±0.04	14.76±0.04	11.
02	17.32±0.01	17.40±0.01	16.92±0.08	16.95±0.06	17.10±0.04	17.18±0.04	17.48±0.05	4.
03	15.76±0.01	15.69±0.00	15.08±0.08	14.87±0.06	14.82±0.04	15.24±0.04	15.43±0.04	9.
04	15.49±0.00	15.29±0.00	14.64±0.08	14.71±0.06	14.80±0.04	14.92±0.04	15.08±0.04	6.
05	14.84±0.00	14.66±0.00	14.59±0.08	14.40±0.06	14.44±0.04	14.89±0.04	15.16±0.04	12.
06	15.20±0.01	15.05±0.00	14.86±0.08	14.89±0.06	14.95±0.03	15.20±0.03	15.26±0.04	20.
07	14.42±0.01	14.34±0.00	14.09±0.08	14.16±0.06	14.30±0.03	14.41±0.03	14.64±0.06	8.
08	16.23±0.04	16.13±0.04	15.67±0.08	15.75±0.06	15.90±0.04	15.94±0.04	16.22±0.05	8.
09	18.67±0.11	18.85±0.19	17.61±0.08	17.82±0.06	17.97±0.04	17.83±0.04	18.34±0.06	3.
10	19.28±0.04	19.15±0.03	18.36±0.08	18.50±0.06	18.52±0.04	18.33±0.04	18.60±0.06	2.
11	18.69±0.03	18.68±0.03	17.51±0.08	17.68±0.06	17.80±0.05	17.70±0.04	17.94±0.06	5.
12	14.85±0.00	14.72±0.00	14.38±0.08	14.29±0.06	14.32±0.04	14.27±0.04	13.97±0.04	23.
13	16.74±0.01	16.71±0.01	16.13±0.08	16.14±0.06	16.24±0.04	16.19±0.04	16.20±0.04	9.
14	17.02±0.01	17.03±0.01	16.66±0.08	16.74±0.06	16.87±0.04	17.03±0.04	17.34±0.05	6.
15	18.07±0.02	18.13±0.02	17.20±0.08	17.36±0.06	17.50±0.04	17.47±0.04	17.81±0.05	5.
16	19.67±0.09	19.91±0.13	18.82±0.08	18.93±0.06	19.01±0.05	18.99±0.05	19.30±0.08	2.
17	17.29±0.02	17.47±0.01	17.16±0.08	17.01±0.06	17.05±0.04	17.52±0.05	17.65±0.06	8.
18	18.39±0.03	18.39±0.02	18.19±0.08	18.33±0.06	18.46±0.04	18.64±0.04	18.96±0.05	3.
19	19.28±0.04	19.42±0.04	17.90±0.08	17.81±0.06	17.76±0.04	17.70±0.04	17.94±0.05	6.
20	19.90±0.04	20.05±0.03	19.46±0.08	19.52±0.06	19.55±0.04	19.70±0.05	20.19±0.08	3.
21	16.89±0.01	16.81±0.01	16.60±0.08	16.59±0.06	16.72±0.04	16.94±0.04	17.17±0.05	7.
22	18.37±0.02	18.57±0.01	17.67±0.08	18.05±0.06	18.24±0.04	18.39±0.04	18.59±0.07	4.
23	18.09±0.03	18.13±0.02	17.27±0.08	17.62±0.06	17.77±0.04	17.97±0.05	18.15±0.08	7.
24	19.33±0.04	19.47±0.03	18.48±0.08	18.93±0.06	19.11±0.05	19.19±0.05	19.29±0.09	4.
25	16.25±0.01	16.25±0.01	15.58±0.08	15.55±0.06	15.66±0.04	15.72±0.04	15.97±0.05	9.
26	16.59±0.02	16.60±0.02	15.82±0.08	15.91±0.06	16.05±0.05	16.07±0.05	16.50±0.07	7.
27	17.40±0.04	17.44±0.01	16.75±0.08	16.94±0.07	17.17±0.07	17.22±0.06	17.54±0.09	5.
28	17.97±0.02	17.89±0.02	16.61±0.08	16.68±0.06	16.76±0.04	16.62±0.04	16.86±0.05	6.
29	17.63±0.03	17.65±0.03	16.57±0.08	16.75±0.07	16.84±0.05	16.69±0.05	16.84±0.09	9.
30	16.23±0.04	16.02±0.03	15.12±0.08	15.21±0.06	15.25±0.04	15.09±0.04	15.17±0.05	11.
31	16.78±0.01	16.63±0.01	15.99±0.08	16.09±0.06	16.30±0.04	16.36±0.04	16.74±0.06	7.
32	17.95±0.05	17.82±0.05	16.94±0.08	16.88±0.06	17.01±0.05	17.10±0.05	17.27±0.06	7.

vidually for each cluster in regions where the contamination of bright nearby objects was minimal.

Table 2 displays the UV and optical photometry of the cluster sample and the corresponding uncertainties, which include the errors from the object count rate, the sky variance, and the zero point calibration.

4.1. UV photometry

The flux density in the FUV and NUV filters was measured within circular apertures given in Table 2, and the median background flux was estimated in annuli of 5 pixel width, chosen in a way to reduce the contamination of nearby sources. Conversion from count rates to the AB photometric system (Oke 1990) was obtained using the zero-points $\mathrm{ZP}^{AB}_{FUV} = 18.82$ and $\mathrm{ZP}^{AB}_{NUV} = 20.08$ (Morrissey et al. 2005). UV magnitudes were corrected for foreground Galactic extinction following Schlegel et al. (1998) before starting the analysis of the cluster SEDs.

4.2. UBVRI and Hα photometry

UBVRI instrumental magnitudes were converted to the standard Johnson and Cousin system using stars from the Massey et al. (2006) catalogue. The colour term in the *UVBRI* transformation (described in Massey et al. 2006) was ignored, as it is smaller than the errors we report. The contribution of the Galactic foreground extinction was also subtracted from the optical magnitudes according to Schlegel et al. (1998).

The continuum emission in the Hα image was removed by subtracting the *R*-band image scaled by a factor 0.40, which was determined from the aperture photometry of 20 field stars in both filters. The calibration factor of 1.79 $\times 10^{-19}$ erg s^{-1} cm^{-2} given in Massey et al. (2007) was applied to the count rates measured within apertures that included the total Hα emission around the cluster. The fluxes are displayed in Table 3. As a further check, Hα fluxes were determined for the same apertures on the map of Hoopes & Walterbos (2000), adopting a calibration factor of 8.2 $\times 10^{-18}$ erg s^{-1} cm^{-2}. The resulting measurements agreed with the LGS map within 5% (1σ).

Hα and oxygen emission lines may significantly contribute to the total flux in the *R*, *V* and *U* bands. We estimated the contamination from [O III] λ5007 and Hα lines to the photometry in the *V* and *R* filters, using the narrowband images provided by LGS. The correction was obtained by subtracting the flux measured in the narrowband image within the same aperture used for the optical photometry (last column in Table 2). We used the calibration factor of 2.11 $\times 10^{-18}$ and 6.41 $\times 10^{-18}$ erg s^{-1} cm^{-2} Å^{-1} for the Hα and [O III] images respectively, as given in Massey et al. (2007). The *U* photometry is affected by the contamination from the [O II] λ3727 line, but the LGS does not provide a narrowband image centred on this wavelength. Thus we multiplied the [O III] narrowband fluxes for the [O II]/[O III] line ratio derived for the clusters in the Rosolowsky & Simon (2008) catalogue. For those without a direct measurement of this ratio, we applied

Table 3. Hα and *Spitzer* IRAC/MIPS photometry of the sample. Flux units are in ergs s^{-1} cm^{-2}.

ID	$F^{0}_{H\alpha}$ 10^{-13} cgs	$\lambda F^{3.6}_{\lambda}$ 10^{-12} cgs	$\lambda F^{4.5}_{\lambda}$ 10^{-12} cgs	$\lambda F^{5.8}_{\lambda}$ 10^{-12} cgs	$\lambda F^{8.0}_{\lambda}$ 10^{-12} cgs	λF^{24}_{λ} 10^{-12} cgs
1	25.29±0.13	6.10±0.74	4.23±0.53	9.73±1.06	24.18±2.51	23.78±2.40
2	4.82±0.15	0.22±0.10	0.17±0.07	0.50±0.11	1.65±0.23	0.75±0.09
3	52.85±1.62	1.20±0.68	1.00±0.37	1.54±0.27	7.76±0.88	6.71±0.69
4	26.33±0.56	2.65±0.38	2.16±0.31	6.43±0.73	16.40±1.71	15.77±1.60
5	61.11±0.36	1.57±0.26	1.37±0.22	2.31±0.31	9.63±1.03	9.85±1.01
6	4.80±0.24	1.92±0.32	1.06±0.20	3.07±0.39	7.04±0.77	3.14±0.33
7	32.64±0.38	1.92±0.31	1.42±0.23	3.90±0.47	26.65±2.75	18.56±1.88
8	11.48±0.34	4.08±0.55	2.51±0.35	10.67±1.16	26.15±2.69	16.17±1.64
9	4.18±0.09	0.42±0.12	0.30±0.09	1.26±0.20	5.10±0.64	2.20±0.24
10	2.51±0.07	0.28±0.09	0.20±0.07	0.76±0.14	3.31±0.40	2.39±0.26
11	2.58±0.06	0.32±0.10	0.22±0.07	0.93±0.16	2.76±0.35	0.75±0.10
12	19.92±0.13	11.96±1.35	7.63±0.88	18.95±1.98	35.46±3.61	24.89±2.51
13	7.29±0.05	1.62±0.28	1.20±0.21	3.12±0.39	7.98±0.87	4.32±0.45
14	3.15±0.08	0.54±0.14	0.37±0.10	1.42±0.21	3.81±0.44	1.89±0.21
15	3.66±0.07	0.42±0.12	0.37±0.10	1.18±0.19	3.29±0.39	5.69±0.59
16	0.72±0.02	0.08±0.05	0.05±0.04	0.21±0.06	1.21±0.17	0.38±0.06
17	5.94±0.09	0.12±0.06	0.10±0.05	0.16±0.06	2.11±0.28	0.58±0.08
18	0.72±0.02	0.10±0.05	0.06±0.04	0.15±0.05	0.46±0.09	0.19±0.03
19	4.13±0.08	0.16±0.07	0.12±0.05	0.29±0.08	2.14±0.27	0.46±0.06
20	0.30±0.01	0.03±0.03	0.02±0.02	0.07±0.04	0.23±0.06	0.09±0.02
21	4.88±0.15	0.17±0.08	0.12±0.06	0.18±0.06	1.30±0.21	0.51±0.08
22	0.68±0.01	0.10±0.05	0.06±0.04	0.15±0.05	0.40±0.08	0.15±0.03
23	1.78±0.04	0.09±0.05	0.07±0.04	0.08±0.04	0.48±0.10	0.13±0.03
24	0.43±0.01	0.08±0.07	0.05±0.04	0.10±0.04	0.23±0.06	0.07±0.02
25	25.56±0.87	4.76±0.60	3.96±0.50	14.34±1.52	39.06±3.99	72.34±7.26
26	15.36±0.34	1.34±0.26	0.92±0.19	5.04±0.60	34.17±3.60	8.75±0.91
27	4.14±0.14	1.54±0.26	1.09±0.19	5.15±0.60	16.57±1.73	8.75±0.90
28	12.52±0.25	1.93±0.31	1.55±0.25	4.39±0.52	12.29±1.33	12.10±1.23
29	6.74±0.23	0.91±0.21	0.63±0.15	3.11±0.40	4.64±0.66	2.70±0.30
30	16.18±0.53	3.32±0.46	2.09±0.31	9.32±1.03	28.48±2.96	11.66±1.19
31	18.67±0.47	1.78±0.29	1.11±0.20	6.18±0.70	45.39±4.63	12.18±1.24
32	1.53±0.06	0.44±0.12	0.28±0.09	1.42±0.21	3.29±0.39	2.20±0.24

an average value of [O II] /[O III] = 1. In some cases this correction was not sufficient to reduce the excess in the U-band photometry.

4.3. IRAC and MIPS (24 μm) photometry

Photometry at 3.6, 4.5, and 5.8 μm was derived through the same apertures used for the UV-optical bands, while the larger apertures chosen for the Hα photometry were adopted to measure 8 and 24 μm fluxes. Uncertainties include Poisson noise photon flux, background fluctuations and a 10% flux calibration uncertainty for both the IRAC (Fazio et al. 2004; Reach et al. 2005) and MIPS bands (Engelbracht et al. 2007). Table 3 displays the fluxes at 3.6, 4.5, 5.8, 8.0, and 24 μm for the sample.

5. SED fitting with CHORIZOS

CHi-square cOde for parameteRized modelling and characterIZation of phOtometry and Spectrophotometry (CHORIZOS) is a χ^2 minimization code that enables one to fit an arbitrary family of spectral energy distributions to a set of photometric and spectrophotometric data (Maíz-Apellániz 2004). It compares an observed set of magnitudes to a grid of model SEDs and calculates the probability for a given model to be consistent with the observed photometry. It allows one to constrain both intrinsic parameters (such as age and metallicity) and extrinsic ones such as extinction law and colour excess. The user selects the SED family and chooses the behaviour of each parameter to be fixed, constrained within a certain range, or to be kept free. The code uses the monochromatic equivalents of $E(B-V)$ and R_V, E(4405-5495) and R_{5495}, where 4405 and 5495 are the assumed central wavelengths in Angstrom of the B and V filters. It allows one to choose between the galactic extinction law of Cardelli et al. (1989), the average LMC and LMC2 laws of Misselt et al. (1999) and the Small Magellanic Curve (SMC) extinction law of Gordon & Clayton (1998). Then a χ^2 analysis is performed to assign a likelihood to each SED as a function of the range of parameters.

The code includes a set of STARBURST99 (Leitherer et al. 1999) instantaneous burst models for a range of ages and metallicities, produced using a Salpeter (1955) stellar initial mass function (IMF) with masses within the range 0.1-100 M$_\odot$. The metallicity of the cluster models was chosen at Z=0.004, 0.008 and 0.02, while the age varied between 1 and 100 Myr. We extinguished the theoretical SEDs with all the available extinction laws using a routine provided with the code.

We ran CHORIZOS for all the objects in our sample using seven magnitudes (from FUV to I bands). We did not include the 3.6 and 4.5 μm IRAC bands in the fitting because the contribution of hot dust emission starts at $\lambda \gtrsim 3$ μm (Carico et al. 1988; Kennicutt et al. 2003) and the STARBURST99 models become inapplicable above that wavelength (Leitherer et al. 1999). A more detailed analysis of the MIR region of the cluster SEDs will be presented elsewhere (Giovanardi et al. 2010, in preparation).

We performed the fitting procedure by setting the metallicity at the values displayed in Table 1, leaving the other parameters

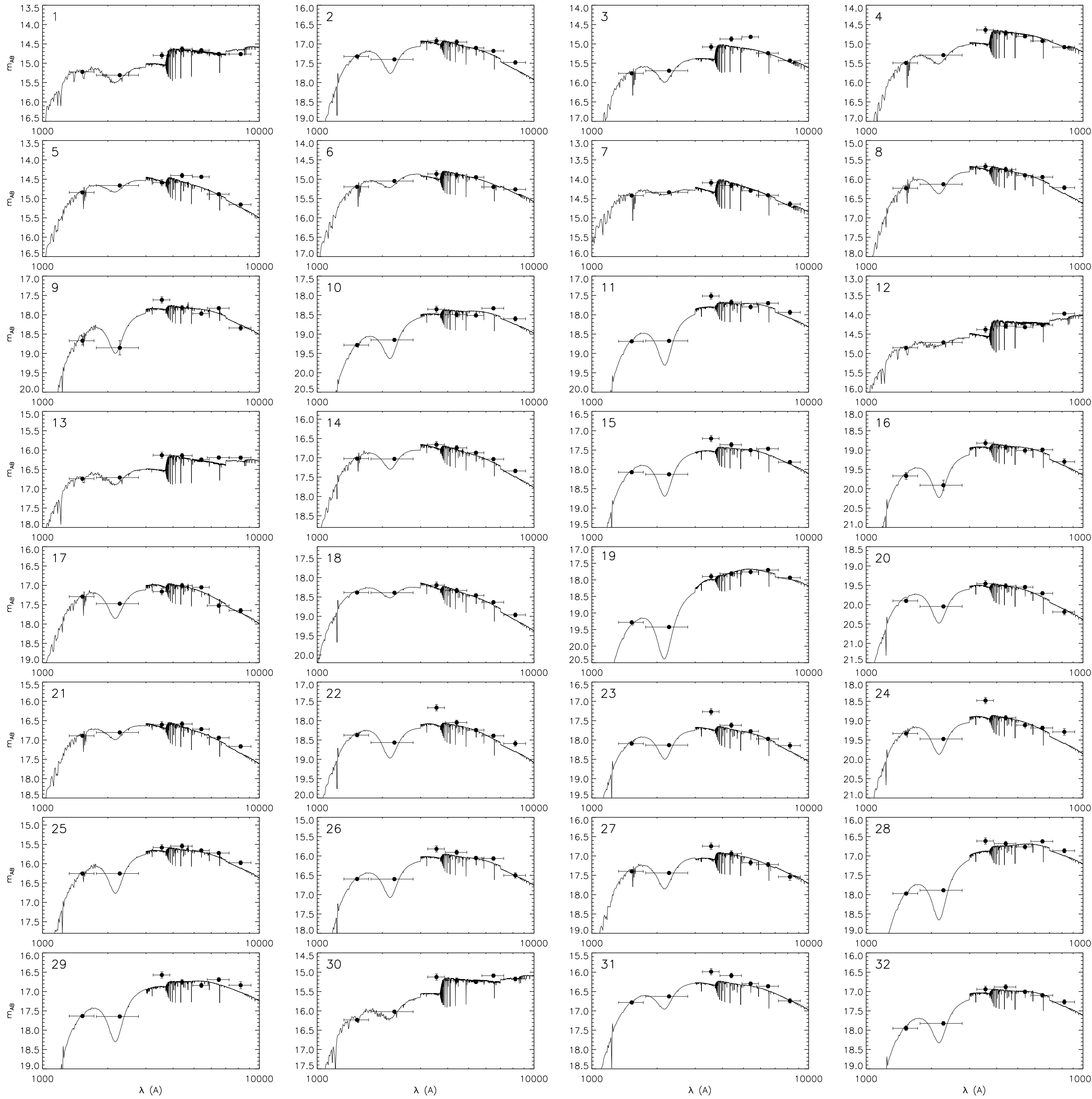

Fig. 2. Output best-fit SEDs in units of AB magnitudes, overlayed on the measured integrated magnitudes from 1000 to 10000 Å. Vertical bars indicate the uncertainty on the photometry, while the horizontal ones show the approximate width of each filter. The numbers at the top-left corners of the plots correspond to the cluster ID given in Table 1.

(i.e. age and intrinsic extinction in M33) unconstrained. Then we reran the code a second time, with a higher resolution grid, to refine the estimate of the parameters. The errors on the age and the extinction are estimated by the procedure. To assess the goodness of the fit, we relied on the value of χ^2 provided by CHORIZOS; on average clusters with $\chi^2 < 10$ were considered as good fits.

Figures 2 and 3 show our SED-fitting results. For each cluster we display the output best-fit SED in units of AB magnitudes from 1000 to 10000 Å overlaid on our measurements to show the quality of the fitting (Fig. 2), and the model SED in flux units (λF_λ, erg s^{-1} cm^{-2}) from 1000 to 3 $\times 10^5$ Å to compare the UV, optical and IR emission of the clusters (Fig. 3). The numbers at the top-left and bottom-right corners of the plots correspond to the cluster ID given in Table 1. The best-fit SEDs overlaid on the observed magnitudes (Fig. 2) show that in some cases the *U* photometry disagrees with the model, despite our attempt to take into account the effects of [OII] line contamination, causing an increase in the value of χ^2. Comparison between the best-fit model SEDs and the MIR photometry (Fig. 3) shows an excess emission at 3.6 μm and 4.5 μm bands, suggesting that this non-stellar emission may be due to a hot dust component.

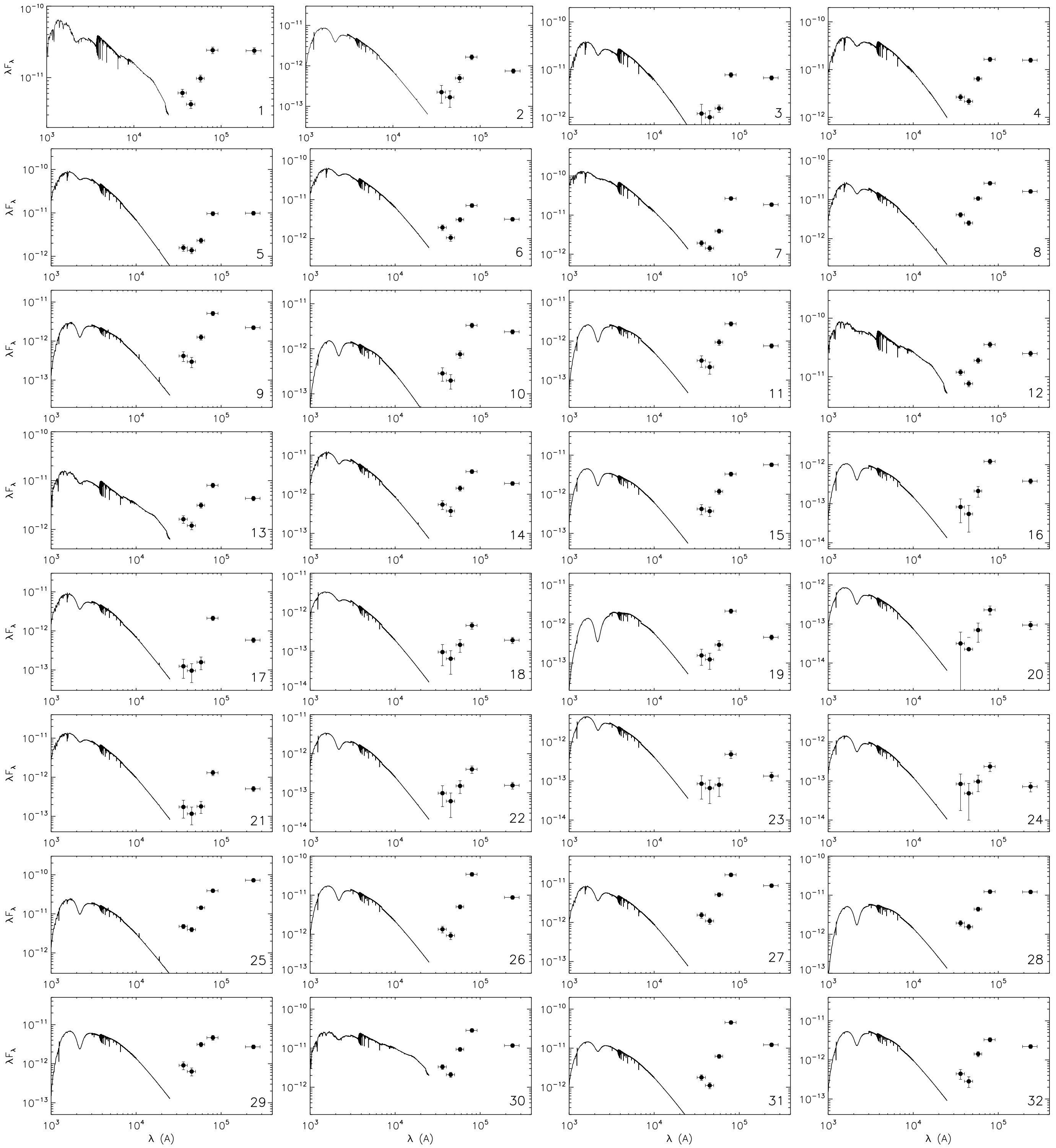

Fig. 3. Model SED for each cluster in flux units (λF_λ, erg s^{-1} cm^{-2}) from 1000 to 3 ×10^{5}Å compared to the *Spitzer* IRAC and MIPS photometry. The numbers at the bottom-right corners of the plots correspond to the cluster ID given in Table 1.

6. Results: comparison of cluster properties

6.1. Ages, masses, sizes, and colours

The SED fittings confirm the young age of the clusters, being younger than ∼15 Myr. The results of the fitting procedure are displayed in Table 4. Uncertainties in age are given in Table 4 and are less than 0.2 (in log years). Variations in the IMF slope from the standard Salpeter value, or stochastic effects in the IMF when sampling small mass clusters, may increase the quoted uncertainties (Cerviño & Luridiana 2004; Corbelli et al. 2009). We will discuss the issue of stochastic fluctuations in Sect. 7.1.

CHORIZOS also determines the bolometric correction to the *V* magnitude for each best-fit model. Knowing the age, metallicity, and the bolometric luminosity, we inferred the stellar mass using the STARBURST99 evolutionary synthesis models. Figure 4 (*top-left* panel) displays the distribution in age and mass of the clusters. It shows that most of the clusters in our sample are found in a very narrow range of ages, while the mass distri-

Table 4. Results from the SED-fitting technique.

ID	log(age) [yr]	A_V mag	$E(B-V)$ mag	$\log(L_{Bol})$ $[L_\odot]$	log(M) $[M_\odot]$
1	6.97±0.01	0.28±0.01	0.13±0.01	6.71±0.01	4.31±0.01
2	6.51±0.14	0.58±0.11	0.26±0.03	6.39±0.08	3.24±0.08
3	6.68±0.09	0.68±0.11	0.30±0.05	7.23±0.01	4.37±0.01
4	6.72±0.03	0.59±0.07	0.24±0.03	6.98±0.05	4.20±0.05
5	6.54±0.03	0.61±0.02	0.23±0.01	7.56±0.01	4.49±0.01
6	6.65±0.15	0.52±0.17	0.23±0.07	6.76±0.12	3.86±0.12
7	6.71±0.02	0.37±0.04	0.14±0.02	7.11±0.03	4.31±0.03
8	6.48±0.16	0.70±0.09	0.29±0.03	6.94±0.07	3.78±0.07
9	6.40±0.10	0.82±0.07	0.35±0.02	6.21±0.03	3.07±0.03
10	6.35±0.21	0.93±0.09	0.39±0.02	6.00±0.10	2.88±0.10
11	6.36±0.13	0.93±0.06	0.41±0.01	6.37±0.04	3.24±0.04
12	6.99±0.04	0.40±0.02	0.16±0.01	6.95±0.01	4.57±0.01
13	7.18±0.04	0.39±0.02	0.16±0.01	6.19±0.01	4.04±0.01
14	6.44±0.16	0.61±0.08	0.25±0.02	6.52±0.07	3.37±0.07
15	6.38±0.16	0.82±0.07	0.36±0.02	6.51±0.05	3.38±0.05
16	6.36±0.15	0.83±0.07	0.37±0.02	5.85±0.04	2.72±0.04
17	6.35±0.13	0.56±0.05	0.26±0.01	6.44±0.03	3.32±0.03
18	6.43±0.17	0.54±0.08	0.22±0.02	5.89±0.07	2.75±0.07
19	6.22±0.12	1.05±0.03	0.51±0.01	6.49±0.01	3.39±0.01
20	6.35±0.14	0.66±0.06	0.30±0.01	5.57±0.04	2.45±0.04
21	6.53±0.16	0.56±0.10	0.24±0.04	6.46±0.09	3.36±0.09
22	6.37±0.09	0.61±0.03	0.28±0.01	6.11±0.02	2.98±0.02
23	6.43±0.13	0.71±0.08	0.30±0.02	6.28±0.06	3.14±0.06
24	6.39±0.10	0.66±0.05	0.30±0.01	5.75±0.03	2.62±0.03
25	6.48±0.14	0.70±0.12	0.32±0.03	6.99±0.07	3.83±0.07
26	6.42±0.14	0.80±0.07	0.34±0.02	7.01±0.06	3.87±0.06
27	6.50±0.17	0.66±0.11	0.30±0.03	6.50±0.09	3.33±0.09
28	6.33±0.14	1.05±0.07	0.46±0.01	6.84±0.03	3.72±0.03
29	6.20±0.11	0.88±0.06	0.40±0.01	6.71±0.03	3.58±0.03
30	7.16±0.11	0.56±0.11	0.27±0.09	6.60±0.02	4.44±0.02
31	6.46±0.17	0.81±0.08	0.33±0.03	6.90±0.07	3.75±0.07
32	6.49±0.14	0.88±0.11	0.38±0.03	6.57±0.07	3.40±0.07

bution encompasses two orders of magnitude, between $\sim 3\times10^2$ and $\sim 4\times10^4$ $M_\odot$. In this and in the following figures we used different symbols (and colours) for clusters within different age bins: filled (blue) dots correspond to ages younger than 3 Myr, (green) squares to clusters with ages in the range 3-8 Myr, while the oldest ones (> 8 Myr) are indicated with (red) triangles.

Observations of Giant Molecular Clouds (GMCs) in different environments indicate that they follow a mass-radius relation $M \propto R^2$ (Larson 1981; Wilson & Scoville 1990; Harris & Pudritz 1994). Thus, once we derived the masses, we checked whether the stellar systems under study follow a similar mass-radius relation or not. As an estimate of the size of the cluster we used the half-light radius measured in the V band. As we show in the *upper-right* panel of Fig. 4, we find a correlation between the half-light radii of the clusters and the mass obtained from the SED fitting, with a slope of 1.5 ± 0.2. The correlation is stronger for clusters with sizes smaller than 10 pc, while the others show a larger scatter around the best-fit line.

Compact star clusters ($R < 10$ pc) with ages between few tens and few hundreds of Myr show a poor correlation between mass and radius (Zepf et al. 1999; Larsen 2004), implying that the GMC mass-radius relation must be broken at a certain stage during the cluster evolution. Larsen (2004) find $M \propto R^{0.1}$ in a sample of relatively young compact clusters (age < 1 Gyr and $R < 10$ pc) in nearby spiral galaxies. On the other hand, cluster complexes with a range of ages more similar to our sample ($\lesssim$ 10 Myr) but larger sizes ($R > 85$ pc) follow a similar mass-radius relation to GMCs, $M \propto R^{2.3}$ (Bastian et al. 2005). Our results seem to indicate that even at scales smaller than those of stellar complexes young stellar systems still display a similar trend to the GMCs, and that the observed stellar densities are representative of the proto-cluster cloud environment.

The *bottom-left* panel of Fig. 4 shows the bolometric luminosity distribution of the clusters, obtained from the SED fitting. The plot of the dereddened $(B-V)_0$ colour as a function of age (*bottom-right* panel) gives an overview of the colour range of the sample. Given their young age, the clusters are characterised by very blue colours and, as expected, "older" clusters are redder than the younger ones.

6.2. Metallicity

The metallicity gradient in M33, from 1 to ~7 kpc is rather shallow (Vilchez et al. 1988; Magrini et al. 2007b), with a central abundance of 12+log(O/H) =8.36± 0.04 and a slope of 0.027± 0.012 dex kpc^{-1} (Rosolowsky & Simon 2008). This can be explained by the global chemical evolution of the M33 disc through an inside-out formation process (Magrini et al. 2007a). In Fig. 5 (*top panel*), the metallicity of the clusters is plotted versus the galactocentric distance, and it is shown that the clusters follow the radial trend found by Rosolowsky and Simon (2008) indicated by the solid line. However, Rosolowsky and Simon (2008) find a scatter of about 0.1 dex in metallicity at a given radius, which is unexplained by the abundance uncertainties only (Rosolowsky & Simon 2008). A possible explanation would be that self-enrichment could be more efficient in more massive

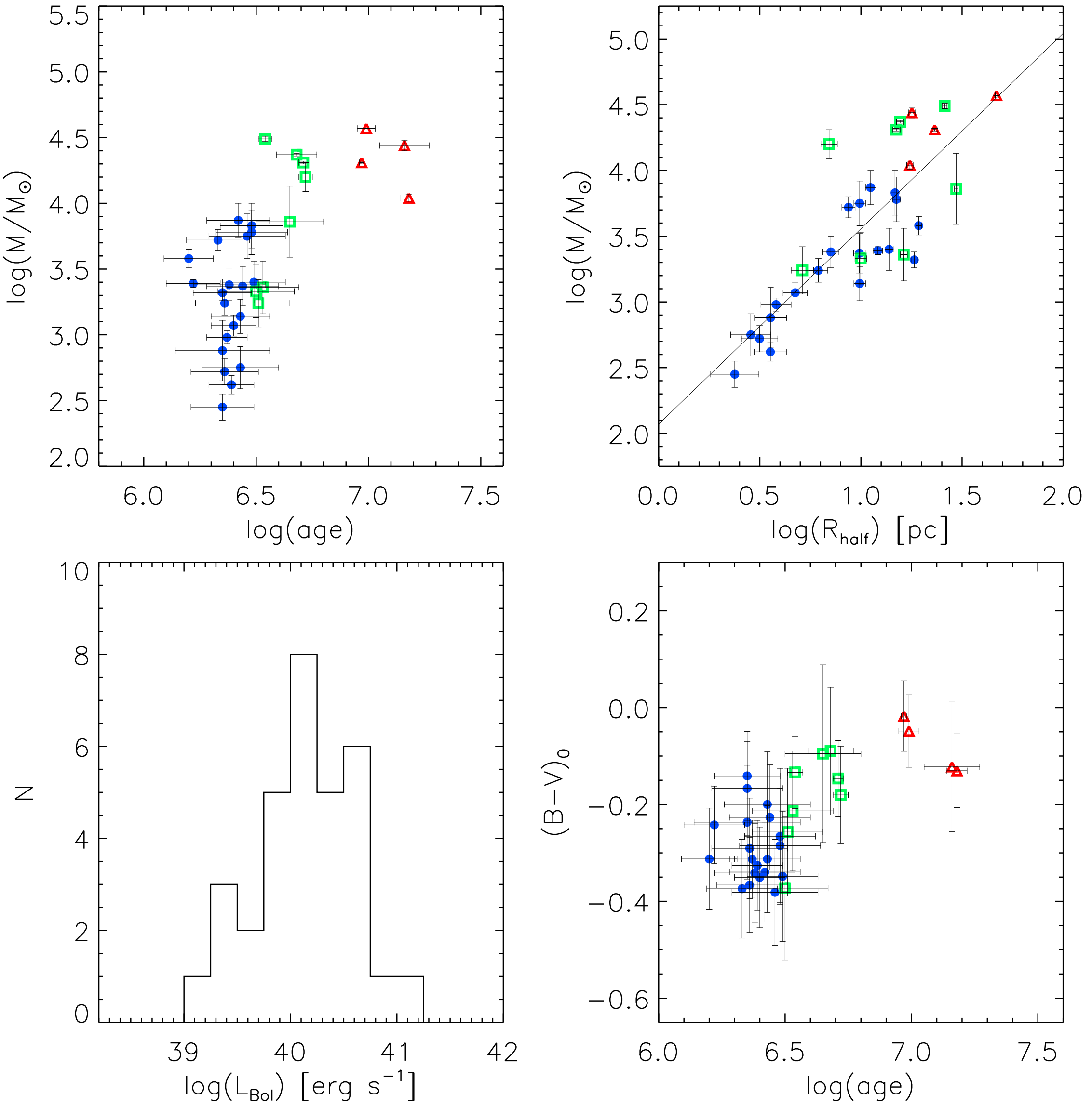

Fig. 4. *Top-left:* cluster ages and masses determined from the SED fitting. *Top-right:* mass versus radius relation: the solid line with a slope of 1.5 provides the best linear fits to the data points. The dotted-line shows the minimum size corresponding to the resolution of the *V*-band image. *Bottom-left:* bolometric luminosity distribution of the sample. *Bottom-right:* $(B - V)_0$ colour distribution as a function of age. The symbols correspond to three different age bins: log(age) $<$ 6.5 (*filled dots*), 6.5 $<$ log(age) $<$ 6.9 (*squares*), log(age) $>$ 6.9 (*triangles*).

clusters, and produce the scatter around the average value. If that is the case, we should find a relation between mass and metallicity in our sample.

The *central panel* of Fig. 5 shows that this correlation is lacking in our sample, indicating that the metal abundance is related to the local environmental properties of the clusters rather than being influenced by the cluster mass. Neither do we find a clear trend between the metallicity and age (*lower panel*); the Spearman correlation coefficient is -0.32, indicating a poor degree of correlation between these two parameters.

6.3. Extinction

Massey & Hutchings (1983) first concluded from the analysis of the IUE spectra of M33 Hii regions that its extinction curve is different from the galactic one, and that it is characterised by a weak 2175 Å hump similar to that of the LMC. Dodorico & Benvenuti (1983) find a similar result after a study of the Hii region IC132. For the brightest Hii region of M33, NGC604, a reddening parameter E(B-V)=0.12 has been obtained assuming a LMC curve (González Delgado & Pérez 2000).

The $E(B-V)$ values we derive for the M33 clusters range between 0.1 and 0.5 mag, corresponding to a visual extinction A_V between 0.3 and 1 mag. Chandar et al. (1999) obtain $E(B - V)$ values between 0.06 and 0.33 mag, with the majority of the clusters being found around 0.1 mag. Park & Lee (2007) derived reddening values between 0.05 and 0.20 mag. Yet both samples are different from ours because they have a large range of ages as mentioned in Sect. 1. The LMC average and LMC2 curves of Misselt et al. (1999) were the ones providing the best fits in the majority of the cases, even though the SMC extinction curve was adopted for one cluster (C400). Additional evidence supporting the choice of either the LMC average or the LMC2 extinction

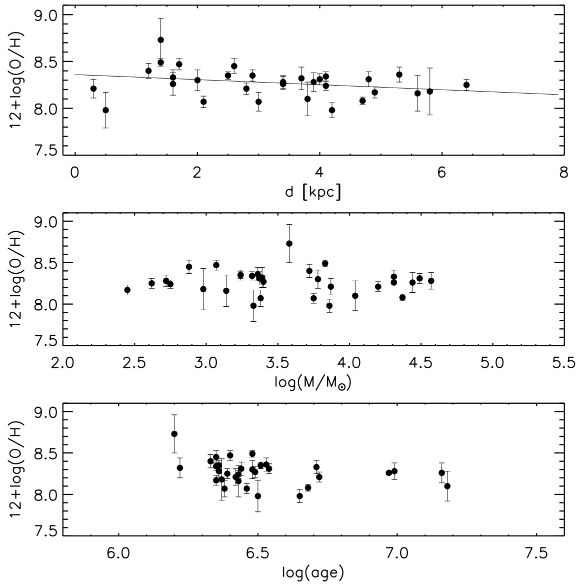

Fig. 5. Cluster oxygen abundance versus galactocentric distance, mass, and age. The solid line in the top panel shows the metallicity radial gradient relation found by Rosolowsky & Simon (2008).

curve comes from the UV colours. The SMC extinction law predicts larger variations in the FUV-NUV colour than what was observed in our sample.

Figure 6 shows that there is a correlation between the cluster age and A_V (*top-left*). Younger clusters are more reddened, because they are still partially embedded in the parent molecular cloud where they formed. A_V does not appear to clearly correlate with the metallicity (*top-centre*), and neither does it correlate with the 8 μm (*top-right*) nor the 24 μm luminosities (*bottom-left*) normalised to the bolometric one. A trend between the extinction and the total hydrogen column density is also lacking (H_2+HI +HII ; see also Sect. 8), as displayed in the *bottom-right* panel.

6.4. Radial gradients

We searched for possible variations of the cluster properties with the galactocentric radius, especially with regard to their UV, Hα or MIR emissions (see Fig. 7).

Neither A_V (*top-left*) nor the L_{FUV}/L_{Bol} ratio (not displayed) show a clear trend with the galactocentric distance. A radial change in A_V would imply a decreasing dust attenuation, as it is found for example in M51 (Calzetti et al. 2005). In this galaxy the UV colour, A_V, and the age of the clusters do vary with the distance, with the clusters becoming younger and less extinct as one moves to the outer regions of the galaxy. Extinction is related to the dust-to-gas ratio, which depends on the metallicity of a galaxy. Because steep metallicity gradients are observed in many galaxies, one would expect that the attenuation properties would also change with the galactocentric distance. The shallow metallicity gradient in M33 (Magrini et al. 2007b; Rosolowsky & Simon 2008) might explain the lack of a clear correlation between A_V, or L_{FUV}/L_{Bol}, and the galactocentric radius.

The $L^0_{H\alpha}/L_{Bol}$ ratio (*top-centre*, Hα corrected for extinction) decreases with galactocentric distance for the youngest clusters (filled dots). However, since the youngest age bin includes several low-mass clusters, this might be due to a selection effect: most of the selected low-mass clusters are at large galactocentric radii in regions that are not too crowded in the Hα map (see the last panel in the figure). We will discuss this in more detail in Sect. 7. Note that the Hα luminosity of the clusters with ages around 10 Myr is more than one order of magnitude higher than what STARBURST99 predicts, implying that subsequent star-formation episodes must have occurred in order to explain the observed Hα emission.

We see a well defined radial trend for the MIR fractional luminosities. Both the L_{24}/L_{Bol} (*top-right*) and the L_8/L^0_{FUV} ratios (*bottom-left*) decrease by at least one order of magnitude at large galactocentric radii, at the edge of the star-forming disc. The MIR emission at 24 μm is mainly due to very small grains with effective radii between 15 and 40 Å (Draine & Li 2007). Variations in the abundance of small grains with respect to big ones at larger radii, or, more generally, a radial gradient in the dust-to gas ratio or in the dust temperature, may also contribute to the decrease of the 24 μm emission (Habart et al. 2001; Abergel et al. 2002; Calzetti et al. 2005). The luminosity at 8 μm is likely dominated by Polyciclic Aromatic Hydrocarbons (PAH) features around star-forming regions excited by the cluster UV radiation, and we find a good correlation between 8 μm and the FUV luminosities of the clusters (Fig. 8). The PAH emission is reduced in low-metallicity objects, but over the small range of metal abundances in our sample there is no clear dependence of the L_8/L^0_{FUV} ratio on the metallicity. At larger radii the volume density of the ISM decreases, therefore one would expect that dust and PAHs may be more efficiently removed from star-forming sites in the outer regions of the disc (Roussel et al. 2005).

The total stellar mass does not seem to be clearly related to the cluster position within the galaxy as shown in the *bottom-right* panel of Fig. 7, even though the smallest mass clusters of the sample ($M < 10^3$ M$_\odot$) are mainly located at large galactocentric distances.

6.5. Bolometric luminosity

The SED-fitting method provides the value of the bolometric luminosity for each cluster, L_{Bol} (see Table 5). We compared this parameter with the bolometric luminosities estimated from observations of the total IR and UV emission, i.e. $L^{obs}_{Bol} = L_{FUV} + L_{NUV} + L_{TIR}/(1-\omega)$, where $\omega \sim 0.5$ is the albedo for a standard dust composition and grain size distribution (Weingartner & Draine 2001).

The sum of the FUV and NUV luminosities provides a measure of the cluster emission below 3000 Å, which is close to the bolometric luminosity if the cluster is young and unobscured by dust (Bell et al. 2005; Thilker et al. 2007). If extinction corrections are unknown, one can use L_{TIR} to estimate the fraction of the UV emission absorbed by the dust. Therefore L^{obs}_{Bol} is considered to provide a good approximation of the bolometric luminosities of young clusters (see Thilker et al. 2007; Corbelli et al. 2009). Verley et al. (2009) have shown that the total IR luminosity in M33 can be estimated from the 24 μm emission and it is approximately $L_{TIR} \sim 12 \times L_{24}$ (see Eq. 4 in Verley et al. 2009).

Figure 9 shows that the model bolometric luminosities are higher than the observed ones for $L^{obs}_{Bol} \lesssim 3 \times 10^{39}$ erg s^{-1}. This difference could be due to two main reasons: a) the assumption of a complete IMF may be incorrect when we consider clusters with bolometric luminosity (and mass) below a certain threshold, leading to an overestimate of the total cluster luminosity; b) the estimated total IR emission of the clusters is lower than the

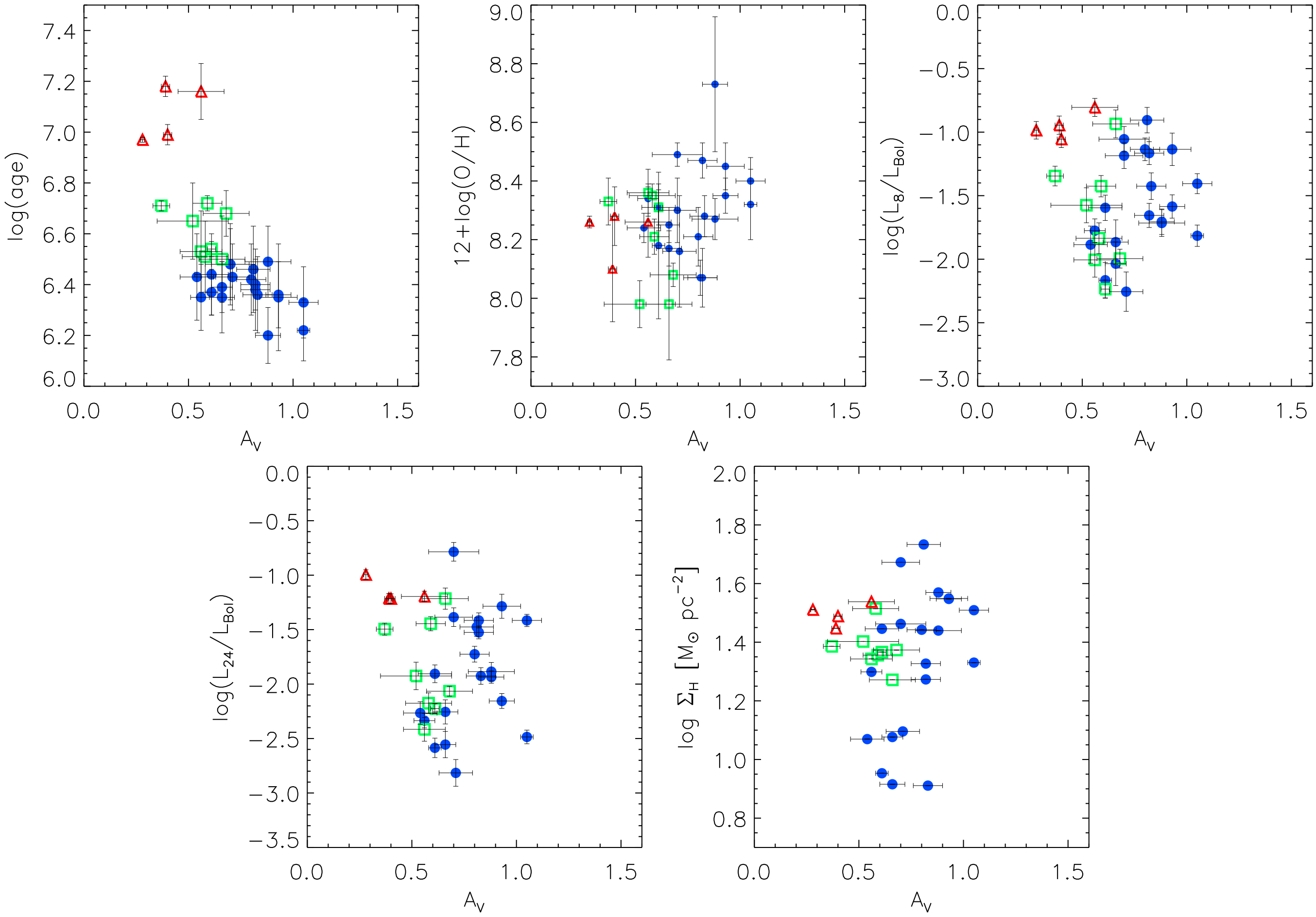

Fig. 6. Visual extinction (A_V) versus age (*top-left*), the measured oxygen abundance (*top-centre*), the ratio of the the 8 μm to the bolometric luminosity (*top-right*), the ratio of the the 24 μm to the bolometric luminosity (*bottom-left*), the total gas density within a region of about 200 pc around the cluster (*bottom-right*). Symbols are the same as for Fig. 4.

amount of energy missing in the non-ionising UV region of the spectrum, implying that there is a deficit of non-ionising radiation in young clusters with bolometric luminosities lower than 3×10^{39} erg s^{-1}. We will discuss these issues in more detail in the next section.

7. The deficit of ionising radiation

In the previous section we pointed out that the total IR emission of the clusters with $\log(L_{Bol}) < 39.5$ is lower than the amount of energy missing in the non-ionising UV region of the spectrum. Here we want to compare the observed Hα luminosity with that predicted by an instantaneous burst model to check whether there is a deficit of UV-ionising radiation in the sample of clusters under study.

We ran STARBUST99 to obtain the expected Hα luminosity of each cluster at the age, metallicity, and mass we determined, and we plot in Fig. 10 the ratio of the extinction-corrected observed Hα luminosity to the model one – $L^0_{H\alpha}/L^{SB99}_{H\alpha}$ – versus the age (*left-panel*) and the mass (*central-panel*) of the clusters. The figures show that this ratio decreases with age and mass, while the *right-panel* shows a shallow radial trend with the galactocentric radius for the youngest clusters. There is a significant discrepancy between the observed and model Hα emission especially in young ($t < 3$ Myr) and low-mass ($\log(M/M_\odot) < 3.5$) systems, for which $L^0_{H\alpha}/L^{SB99}_{H\alpha}$ is less than 0.5, or -0.3 in logarithmic units. This would imply that more than 50% of the ionising flux is missing from these clusters, a higher percentage than what was found in other studies (see Sect. 7.3).

The error bars in Fig. 10 show how the ratio of Hα luminosities varies if one takes into account the uncertainties of the best-fit ages (Table 4). The upper errors bars are larger for clusters older than 2.5-3 Myr, because the model Hα emission rapidly decreases after this epoch. For the youngest clusters ($t < 3$ Myr), the mean $L^0_{H\alpha}/L^{SB99}_{H\alpha}$ ratio is $0.19^{+0.17}_{-0.002}$, while for those with an age between 3 and 8 Myr the mean is $L^0_{H\alpha}/L^{SB99}_{H\alpha} = 0.65^{+0.83}_{-0.22}$. On the other hand, clusters older than 8 Myr (triangles in Fig. 10) are very luminous at Hα wavelengths for their age, because $L^0_{H\alpha}$ is more than 10 times higher than the prediction of simple stellar population models. It is likely that in these cases the assumption of an instantaneous burst is incorrect and an extended star-formation activity is required to explain the observed Hα emission.

Hence, even taking into account the uncertainties of the cluster ages, the missing fraction of ionising radiation is rather large in young clusters, and we examine four different hypotheses to explain this issue.

First we discuss how the incomplete sampling of the IMF and statistical fluctuations can affect the prediction of cluster luminosities. Then we consider the effects related to the cluster environment such as dust absorption and photon-leakage (i.e. a large fraction of UV radiation escapes the HII region). Finally we

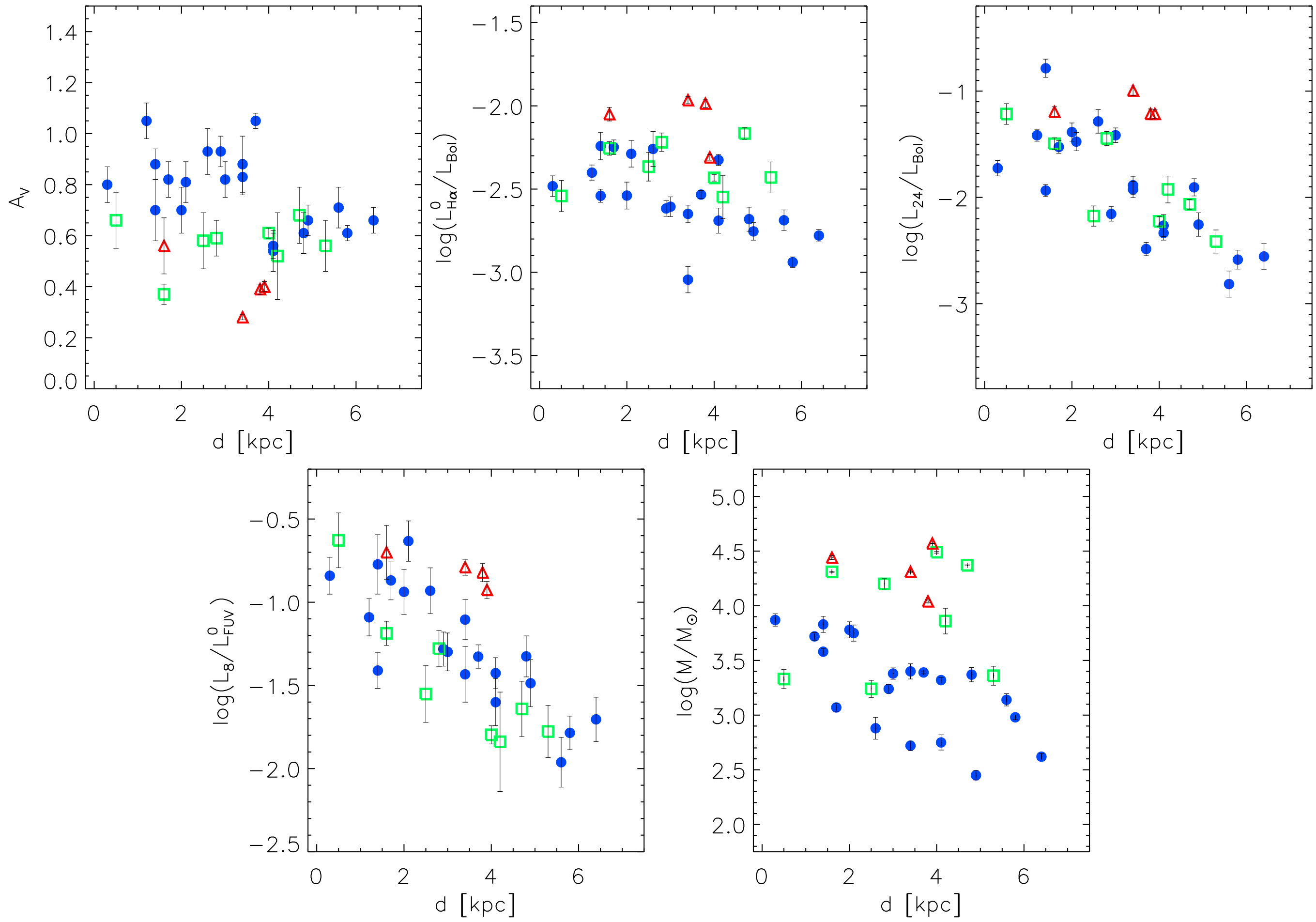

Fig. 7. Cluster galactocentric distance versus A_V (*top-left*), the $L^0_{H\alpha}/L_{Bol}$ ratio (Hα corrected for extinction, *top-centre*); the L_{24}/L_{Bol} ratio (*top-right*); the L_8/L^0_{FUV} ratio (FUV corrected for extinction, *bottom-left*); the total stellar mass (*bottom-right*). Symbols are the same as for Fig. 4.

briefly discuss whether the delayed formation of the most massive stars or a truncated IMF can offer alternative explanations for the low Hα luminosity observed in very young clusters.

7.1. The consequence of sampling effects in the IMF

The library of models that we used for the SED fitting assumes a standard Salpeter IMF, fully populated up to a high-mass end of 100 $M_\odot$. It is possible that the difference between the expected and observed Hα luminosities in the youngest clusters is because we are overestimating the number of massive stars owing to the incompleteness of the IMF at the high-mass end.

Incomplete sampling is often neglected, and it is assumed that the mass spectrum of stellar clusters can be represented by a continuous function given by the underlying IMF. On the other hand, numerical simulations of synthetic clusters by a stochastic generation of stars show that this assumption is correct for massive systems ($M > 10^4$ $M_\odot$), whereas large deviations at the high-mass end occur for small clusters (Corbelli et al. 2009). The critical mass below which statistical fluctuations become relevant depends on the cluster age and metallicity, and on the spectral range under study (Cerviño et al. 2002, 2003). For example, according to Fatuzzo & Adams (2008), sampling effects dominate in the FUV range when extinction corrected FUV fluxes are below 10^{39} erg s^{-1}. Most of our selected objects lie above this threshold, but the situation might change if we are interested in the UV ionising radiation, because it has a steeper dependence on the stellar mass than the non-ionising continuum. Hence, to estimate the Hα luminosities of the smallest clusters in our sample, sampling effects need to be considered.

In Fig. 11 we show how the median bolometric (diamonds) and Hα (stars) luminosities of a cluster depend on its mass. The simulation was carried out as described in Corbelli et al. (2009), but here we assumed a maximum stellar mass of 100 $M_\odot$ to be consistent with the fitting procedure used in this paper. The luminosities are computed for zero-age main-sequence stars.

Low-mass clusters have a larger dispersion around the median Hα luminosity than around the bolometric luminosity. Moreover, $L_{H\alpha}$ deviates considerably from a simple linear relation (solid line) at masses lower than 1450 $M_\odot$. Below this limit the IMF is not fully populated at its high-end, and the stronger dependence of $L_{H\alpha}$ on the stellar mass implies that the mean value of $L_{Bol}/L_{H\alpha}$ increases, despite the occasional presence of outliers.

The IMF statistical fluctuations introduce a large dispersion in the observable properties of the low-mass clusters ($M < 1450$ $M_\odot$), when the linear relation between cluster mass and $L_{H\alpha}$ breaks down. Thus, to account for the incomplete sampling of the IMF in these clusters, we will use the Hα luminosity and the dispersions derived with our simulation (see Fig. 11). Note that all clusters with $M < 1450$ $M_\odot$ in our sample are quite

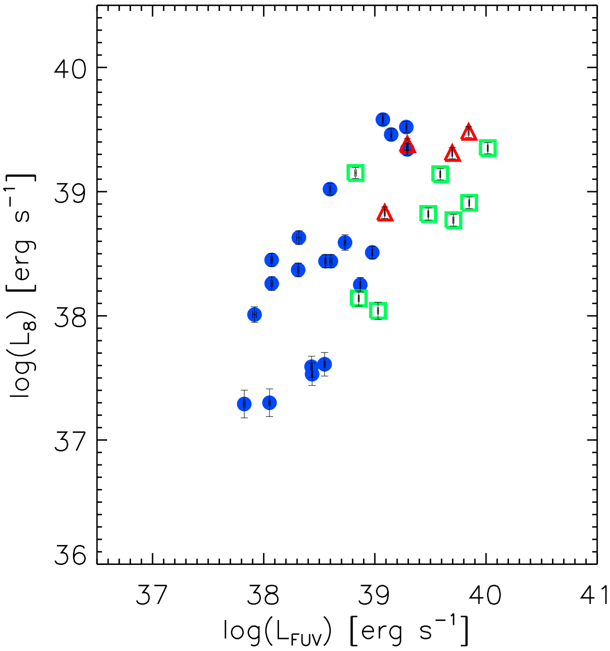

Fig. 8. FUV luminosity, L_{FUV}, versus 8 μm luminosity, L_8, for the cluster sample. Symbols are the same as for Fig. 4.

young, hence their expected Hα emission is well represented by the simulated data in Fig. 11. For older and massive clusters we shall use the luminosities obtained for a complete IMF (STARBURST99) with the dispersion given by our simulation. Cerviño et al. (2003) have shown that the minimum mass below which we expect stochastic effects, as well as the dispersion around the mean or median value, have a very weak dependence on the cluster age during the first 10 Myr.

The expected Hα luminosities of low-mass clusters are lower when stochastic effects are considered, as shown in Fig. 12. The error bars in the figure include both the dispersion of the model Hα luminosity and the uncertainty due to the error on the age of the clusters. The mean $L^0_{H\alpha}/L^{mod}_{H\alpha}$ ratio[1] for the youngest clusters (t < 3Myr) is $0.30^{+0.8}_{-0.07}$. Therefore, taking into account the stochastic effects reduces the discrepancy between the expected and observed values, but the large uncertainties prevent us to draw any firm conclusions on how the missing Hα flux depends on the cluster mass, age, or galactocentric radius, as we show in Fig. 12.

7.2. Dust absorption

Dust within or around the cluster can absorb the UV photons emitted by the hot massive stars, reducing the amount of ionising radiation, and contributing to the lack of observed Hα photons.

The good spatial correlation between 24 μm and Hα emissions shows that the dust is predominantly heated by OB stars within the HII regions. The *Spitzer* resolution at 70 and 160 μm is not sufficient to resolve our sources, and we estimated the total IR luminosity from the 24 μm emission following Verley et al. (2009). This agrees with what other studies found when the IR luminosity is dominated by emission at wavelengths longer than 24 μm. Nevertheless, the total IR luminosities are lower than what is required by the modest extinctions obtained from the SED-fitting procedure. Some additional contribution to L_{TIR} might come from a hot dust component heated by young stars in these sources. The SED indicates an excess above the expected stellar emission at 3.6 and 4.5 μm. However, given the limited MIR emission detected around the clusters and, more generally, the low dust content of M33, it is difficult to explain the missing ionising radiation as an effect of dust absorption only (see Sects. 6.4 and 6.5), even though this mechanism would explain the observed trend with cluster age.

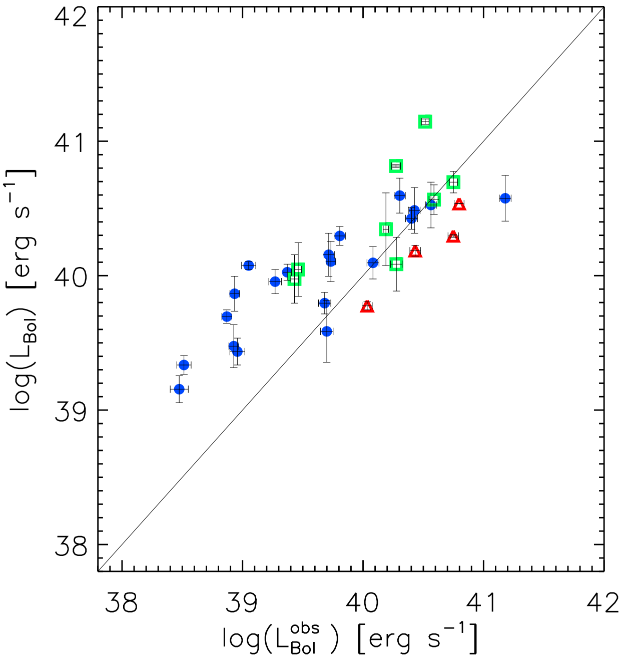

Fig. 9. Comparison between the cluster bolometric luminosity determined from the SED spectral fitting (y-axis) and the observed bolometric luminosity derived by adding the measured FUV, NUV, and the total IR luminosity estimated following Verley et al. (2009) as $L_{TIR} \sim 12\times L_{24}$. Symbols are the same as for Fig. 4.

On the other hand, the way dust is distributed within or around the HII regions may produce different attenuation of the emitted light, and the usual assumption of a homogeneous dust screen may lead to an underestimation of the effects of dust extinction (Petersen & Gammelgaard 1997). For example, a clumpy dust distribution would explain the missing fraction of ionising radiation (40%) observed in the super star clusters of SBS 0335-052 (Reines et al. 2008). A more detailed analysis of the dust properties for these clusters, taking into account more complex dust distributions, will be addressed elsewhere (Giovanardi et al. 2010, in preparation).

7.3. Leakage of UV photons

UV photons not absorbed by dust grains can escape from the star-forming region and explain the origin of the extended diffuse UV emission observed by GALEX in the M33 disc (Thilker et al. 2005).

The importance of taking into account the leakage of ionising photons from HII regions has been increasingly discussed in recent years, especially after the discovery of the diffuse ionised gas (DIG) in the ISM of the Milky Way (Reynolds et al. 1974), and in the discs of other spiral galaxies (Greenawalt et al. 1998). The DIG components of galaxies such

---

[1] Note that to derive the mean ratio we discarded the two lowest mass clusters with the largest error bars.

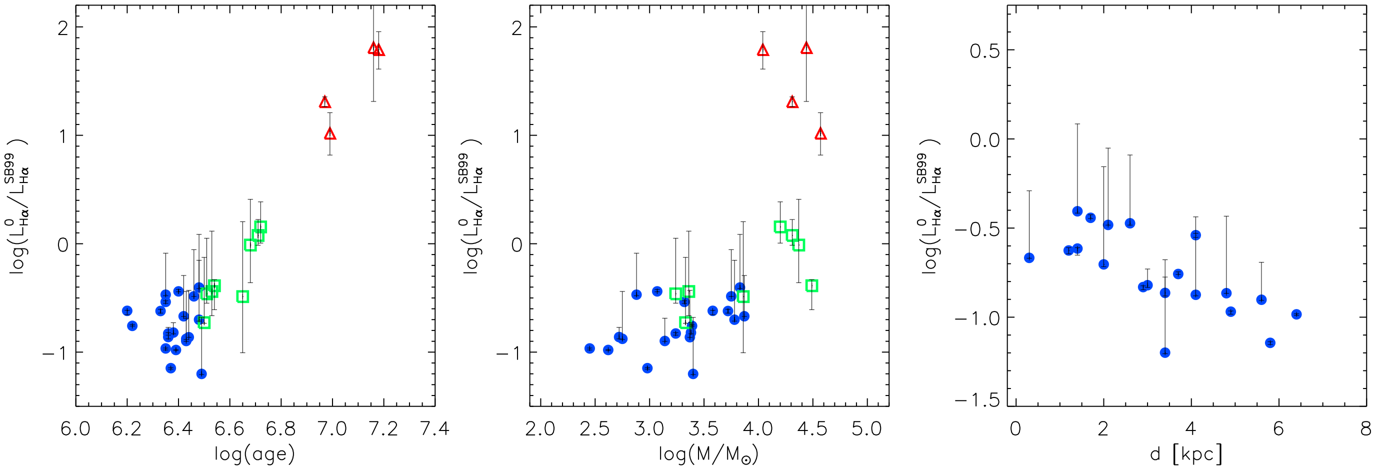

Fig. 10. Ratio of the observed (extinction corrected) to the model Hα luminosity determined with STARBURST99 vs. the age of the clusters (*left-panel*), the mass of the clusters (*central-panel*), and the galactocentric distance for clusters with log(age) < 6.5 (*right-panel*). The error bars give the range of the Hα luminosity predicted by STARBURST99 for each cluster due to uncertainty on the age. Symbols are the same as for Fig. 4.

as M31 (Walterbos & Braun 1996), the LMC (Oey & Kennicutt 1997, 1998), the SMC (Relaño et al. 2002), amount to the 30% and 50% of the total Hα luminosity. Studies of field OB stars in M33 (Hoopes & Walterbos 2000, 2003) have given evidence that at least 20% - 30% Lyman continuum photons must be able to escape from the H ii regions in this galaxy. Nonetheless, there is still a debate about whether the energy budget of photons leaking out of H ii regions is sufficient to ionise the DIG or if additional mechanisms should be considered (Voges et al. 2008).

Theoretical models have shown that the amount of leakage is regulated by the structure and clumpiness of the ISM (Miller & Cox 1993; Wood & Mathis 2004). Inhomogeneities in the medium favour the leakage of radiation because the presence of low-density regions may increase the mean free path of the photons (Voges et al. 2008; Reines et al. 2008). The leakage also depends on the spectrum of the ionising radiation, and on the evolutionary stage of the cluster, with the fraction of escaping photons being larger when stars experience a hard Wolf-Rayet phase, which occurs, depending on the mass and metallicity of a star, between 3 and 6 Myr (Castellanos et al. 2002).

Relating the leakage of ionising photons to the beginning of the W-R phase (Castellanos et al. 2002) may explain the age-dependence of the $L^0_{H\alpha}/L^{SB99}_{H\alpha}$ ratio for clusters older than 3 Myr, but the issue would still remain open for the youngest systems.

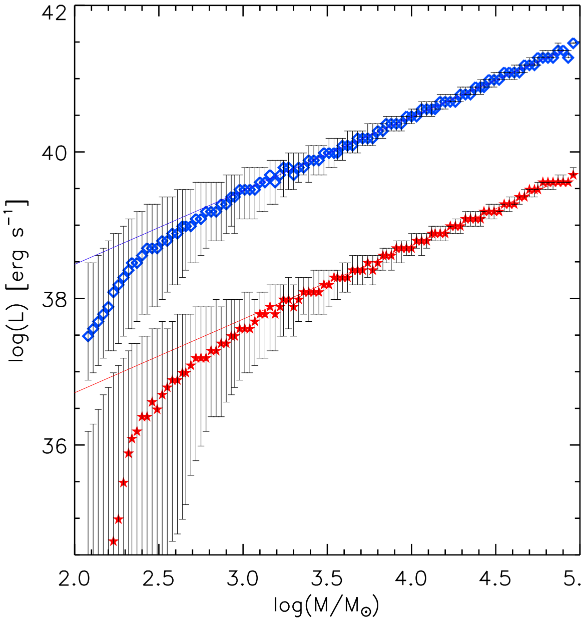

Fig. 11. Expected median bolometric (diamonds) and Hα (stars) luminosity of stellar clusters as a function of cluster mass and their corresponding uncertainties.

7.4. Deficiency or delayed formation of massive stars

The previous considerations cast some doubts on leakage and dust absorption as the only processes causing the deficiency of ionising radiation.

If the star-formation process is not instantaneous, clusters might reach their expected Hα luminosity only after all stars have formed, especially the most massive ones, which determine the cluster Hα luminosity rather than the total mass. Massive stars might form later during the cluster evolution either because they need particular physical conditions and processes to take place (Palla 2005) or because the time-scale for the gas to collapse is longer in a low-density environment such as the disc of M33 (Elmegreen 1999). Therefore, the delayed formation of the most massive stars appears as an interesting and promising way to explain why only very young clusters are underluminous in Hα, and this should be investigated in detail in future work. Particularly, it would be interesting to know whether the excess of Hα emission in the oldest clusters could also be explained by this scenario without the assumption of multiple burst events.

A strong deficiency of massive stars compared to what is predicted by a stochastically sampled IMF should also be considered. For example, truncated models of the stellar IMF (Meurer et al. 2009; Pflamm-Altenburg et al. 2009, and references therein) predict lower cluster luminosities than stochastically sampled models (Corbelli et al. 2009). This is because truncated models link the cluster mass to the most massive stars that can form in a cluster, without considering the occasional presence of outliers. The IMF over the whole galaxy in this case would deviate from the power law assumed in each cluster, and

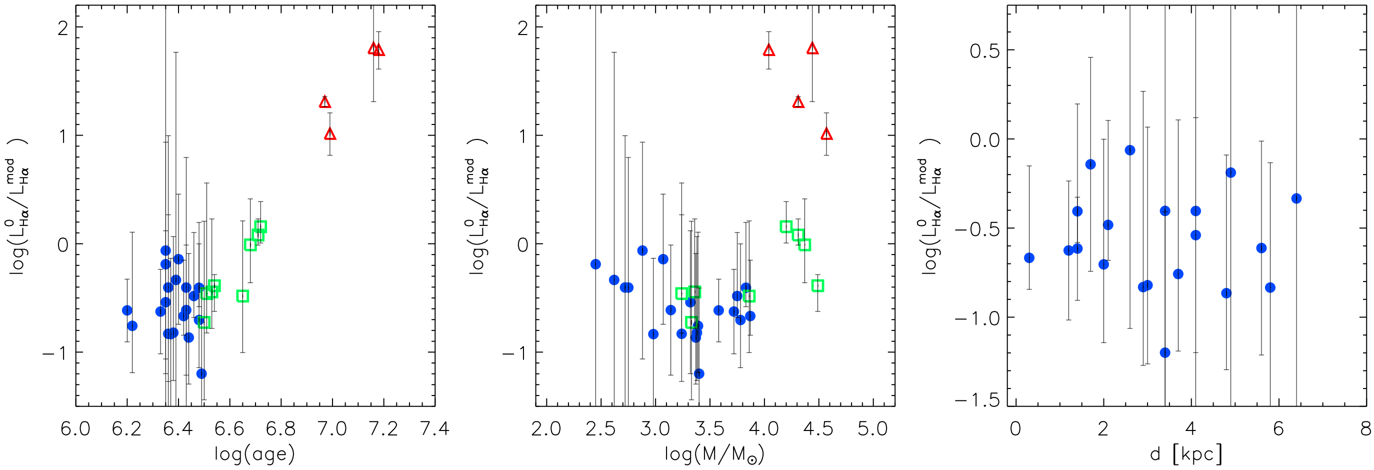

Fig. 12. Ratio of the observed (extinction corrected) to the model Hα luminosity vs. the age of the clusters (*left-panel*), the mass of the clusters (*central-panel*), and the galactocentric distance for clusters with log(age) < 6.5 (*right-panel*). In these plots, the model Hα luminosities of clusters with masses M < 1450 M$_\odot$, were determined with the simulations described in the text, taking into account the incomplete sampling of the IMF. The error bars include both the dispersion of the model Hα luminosity and the uncertainty due to the error on the age of the clusters. Symbols are the same as for Fig. 4.

it will be steeper. Assessing the details of the IMF in M33 and its variance requires the availability of deep colour-magnitude diagrams for the stellar members of each cluster. This is difficult to attain in compact young clusters and is clearly beyond the scope of this study.

8. The gaseous environments of young clusters

Finally, we investigated whether the mass of young clusters is related to the surface density of the different phases of the surrounding ISM (ionised, atomic, molecular gas).

As described in Sect. 2.4, the spatial resolution of the CO and HI maps is 13″and 24″× 48″respectively. Thus, the size of the clusters (see Table 2) is smaller than the resolution of the CO images for roughly half of the objects in our sample, while none of the clusters can be resolved with the beam size of the 21-cm map. For this reason we limit our analysis to areas of the ISM that are larger than the clusters. Using an aperture equal to the lowest resolution gas map (HI) i.e. of 24 arcsec, centred on the optical position of each object, we measured the gas surface densities associated with it.

Figure 13 shows the measured surface density of the different gaseous components as well as the total gas surface density compared to the cluster stellar mass. There is no trend with cluster age, the surface density of the surrounding ISM is not affected by the early stages of cluster evolution. The ionised gas seems to better correlate with the cluster mass (as expected, since the most massive clusters have a higher number of ionising photons). Concerning the HI gas, one can only infer from the figure that the majority of the clusters are found in a narrow regions of surface density ($N_{HI} = 1 \div 3 \times 10^{21}$ cm^{-2}), which is no big surprise given the rather flat HI distribution in the M33 disc. Clusters are born in correspondence to HI filaments, but there is no clear connection between the stellar mass and the gas surface density (Verley et al. 2010).

The *bottom-right* panel of Fig. 13 shows the sum of all gaseous components (ionised, atomic, molecular) versus the stellar mass. It shows that the gaseous environment of these clusters is dominated by the atomic component. For a change of two orders of magnitude in cluster mass there is only half an order of magnitude change in the total gas column density. Because the scatter of this correlation is large, as Verley et al. (2010) have already pointed out, the gas surface density is not the only parameter which determines the star-formation rate and the mass of the newly born clusters.

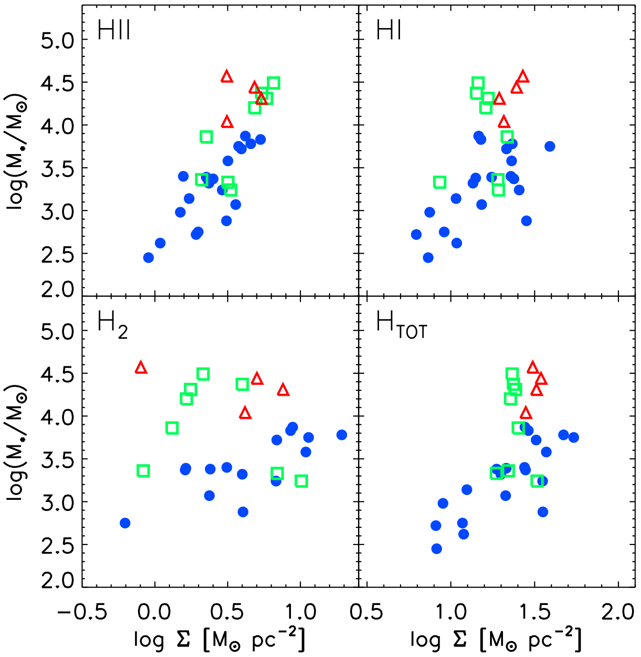

Fig. 13. Surface density of ionised (*top-left*), atomic (*top-right*), molecular (*bottom-left*), and total (*bottom-right*) hydrogen as a function of the stellar mass of the cluster. Symbols and colour codes are the same as for Fig. 4.

9. Summary and conclusions

We analysed multi-wavelength observations of a sample of young star clusters and associations in M33 combining UV

(GALEX), optical (*UBVRI*), and MIR (*Spitzer*/IRAC-MIPS), 3-mm (BIMA-FCRAO) and 21-cm (WSRT) observations. The UV and optical data sets were used to derive their age and mass, and the line-of-sight extinction by fitting the measured SEDs to a set of single-burst stellar population models. The model SEDs were reddened using various extinction laws (Milky Way, LMC, SMC), and the best-fit solutions were obtained with the LMC laws.

We find ages between 2 and 15 Myr and stellar masses between $3{\times}10^2$ and 4×10^4 $M_\odot$. The extinction towards these stellar systems, A_V varies between 0.3 and 1 mag, indicating that they are not highly obscured even in an early evolutionary phase. As expected, older clusters are less extinct than younger ones. We also find a correlation between mass and radius with $M \propto R^{1.5\pm0.2}$. There is no clear trend between extinction and other parameters such as metallicity or total gas surface density. The fractional luminosities at 8 μm and 24 μm decrease with the galactocentric distance, suggesting a lower PAHs and small-grain abundance in the outer regions of the galaxy. A comparison between the model SEDs and the *Spitzer*/IRAC fluxes shows an excess emission at 3.6 μm and 4.5 μm, which may be due to a hot dust component, heated by the ionising radiation of the cluster massive stars.

We find a discrepancy between the observed Hα luminosity and that expected from population synthesis models, especially in young (< 3 Myr) and low-mass ($M < 3 \times 10^3$ $M_\odot$) clusters. The ratio of the observed-to-model Hα luminosity increases with cluster age and ranges between 20% and 90%. We showed that this difference can be reduced but not removed if one takes into account the uncertainties of the age from the SED-fitting procedure and the stochasticity of the IMF at the high mass-end. Similarly, the gap between the best-fit bolometric luminosity (derived assuming a fully sampled IMF) and the total observed luminosity (UV and IR) cannot be fully explained if only a stochastically sampled IMF is considered. We then discussed other possible scenarios:

1. Absorption of Lyman continuum photons by dust in Hii regions cannot fully explain this discrepancy because the IR emissions inferred from the 24 μm luminosity is generally lower than expected from the derived extinction. This suggests that UV continuum photons are missing, but not because of dust absorption only.
2. The escape of UV ionising and non-ionising photons from the Hii region because of a clumpy and porous ISM is a likely scenario that would be supported by the large UV and Hα diffuse fractions observed in this galaxy.
3. Finally we discussed the possibility of a delayed formation of the most massive stars in these clusters as a consequence of the increase in the observed-to-expected Hα luminosity ratio with age and mass. Because the oldest clusters in our sample are also the most massive ones, a stronger suppression of massive star formation in low-mass systems than what is predicted by a stochastically sampled IMF would also alleviate the problem.

Finally, we analysed the surface density of the gas (ionised, atomic, and molecular) in a region about 200 pc wide around the cluster. A marginal correlation only is found between the cluster mass and the total gas surface density, implying that on these large scales this is not the only parameter that determines the total mass of stars.

Acknowledgements. We thank the anonymous referee for the comments and suggestions that contributed to improve the paper. This work is based on observations made with the NASA Galaxy Evolution Explorer and with the *Spitzer* Space Telescope. GALEX is operated for NASA by the California Institute of Technology under NASA contract NAS5-98034. The *Spitzer* Space Telescope is operated by the Jet Propulsion Laboratory, California Institute of Technology under a contract with NASA. This research draws upon data provided by *The Resolved Stellar Content of Local Group Galaxies Currently Forming Stars*, PI: Dr. Philip Massey, as distributed by the NOAO Science Archive. NOAO is operated by the Association of Universities for Research in Astronomy (AURA), Inc. under a cooperative agreement with the National Science Foundation.

References

Abergel, A., Bernard, J. P., Boulanger, F., et al. 2002, A&A, 389, 239
Bastian, N., Gieles, M., Efremov, Y. N., & Lamers, H. J. G. L. M. 2005, A&A, 443, 79
Bell, E. F., Papovich, C., Wolf, C., et al. 2005, ApJ, 625, 23
Boulesteix, J., Courtes, G., Laval, A., Monnet, G., & Petit, H. 1974, A&A, 37, 33
Buckalew, B. A., Kobulnicky, H. A., Darnel, J. M., et al. 2006, ApJS, 162, 329
Calzetti, D., Kennicutt, Jr., R. C., Bianchi, L., et al. 2005, ApJ, 633, 871
Cardelli, J. A., Clayton, G. C., & Mathis, J. S. 1989, ApJ, 345, 245
Carico, D. P., Sanders, D. B., Soifer, B. T., et al. 1988, AJ, 95, 356
Castellanos, M., Díaz, Á. I., & Tenorio-Tagle, G. 2002, ApJ, 565, L79
Cerviño, M. & Luridiana, V. 2004, A&A, 413, 145
Cerviño, M., Luridiana, V., Pérez, E., Vílchez, J. M., & Valls-Gabaud, D. 2003, A&A, 407, 177
Cerviño, M., Valls-Gabaud, D., Luridiana, V., & Mas-Hesse, J. M. 2002, A&A, 381, 51
Chandar, R., Bianchi, L., & Ford, H. C. 1999, ApJS, 122, 431
Chandar, R., Bianchi, L., & Ford, H. C. 2001, A&A, 366, 498
Corbelli, E., Verley, S., Elmegreen, B. G., & Giovanardi, C. 2009, A&A, 495, 479
Courtes, G., Petit, H., Petit, M., Sivan, J.-P., & Dodonov, S. 1987, A&A, 174, 28
Deul, E. R. & van der Hulst, J. M. 1987, A&AS, 67, 509
Dodorico, S. & Benvenuti, P. 1983, MNRAS, 203, 157
Draine, B. T. & Li, A. 2007, ApJ, 657, 810
Elmegreen, B. 1999, in Astronomical Society of the Pacific Conference Series, Vol. 187, The Evolution of Galaxies on Cosmological Timescales, ed. J. E. Beckman & T. J. Mahoney, 145–163
Engargiola, G., Plambeck, R. L., Rosolowsky, E., & Blitz, L. 2003, ApJS, 149, 343
Engelbracht, C. W., Blaylock, M., Su, K. Y. L., et al. 2007, PASP, 119, 994
Fatuzzo, M. & Adams, F. C. 2008, ApJ, 675, 1361
Fazio, G. G., Hora, J. L., Allen, L. E., et al. 2004, ApJS, 154, 10
Gil de Paz, A., Boissier, S., Madore, B. F., et al. 2007, ApJS, 173, 185
González Delgado, R. M. & Pérez, E. 2000, MNRAS, 317, 64
Gordon, K. D. & Clayton, G. C. 1998, ApJ, 500, 816
Gordon, S. M., Duric, N., Kirshner, R. P., Goss, W. M., & Viallefond, F. 1999, ApJS, 120, 247
Greenawalt, B., Walterbos, R. A. M., Thilker, D., & Hoopes, C. G. 1998, ApJ, 506, 135
Habart, E., Verstraete, L., Boulanger, F., et al. 2001, A&A, 373, 702
Harris, W. E. & Pudritz, R. E. 1994, ApJ, 429, 177
Heyer, M. H., Corbelli, E., Schneider, S. E., & Young, J. S. 2004, ApJ, 602, 723
Hodge, P. W., Skelton, B. P., & Ashizawa, J., eds. 2002, Astrophysics and Space Science Library, Vol. 221, An Atlas of Local Group Galaxies
Hoopes, C. G. & Walterbos, R. A. M. 2000, ApJ, 541, 597
Hoopes, C. G. & Walterbos, R. A. M. 2003, ApJ, 586, 902
Kennicutt, Jr., R. C. 1998, ApJ, 498, 541
Kennicutt, Jr., R. C., Armus, L., Bendo, G., et al. 2003, PASP, 115, 928
Larsen, S. S. 2004, in Astronomical Society of the Pacific Conference Series, Vol. 322, The Formation and Evolution of Massive Young Star Clusters, ed. H. J. G. L. M. Lamers, L. J. Smith, & A. Nota, 19–+
Larson, R. B. 1981, MNRAS, 194, 809
Leitherer, C., Schaerer, D., Goldader, J. D., et al. 1999, ApJS, 123, 3
Ma, J., Zhou, X., Chen, J., et al. 2002, AJ, 123, 3141
Ma, J., Zhou, X., & Chen, J.-S. 2004, Chinese Journal of Astronomy and Astrophysics, 4, 125
Ma, J., Zhou, X., Kong, X., et al. 2001, AJ, 122, 1796
Magrini, L., Corbelli, E., & Galli, D. 2007a, A&A, 470, 843
Magrini, L., Corradi, R. L. M., Mampaso, A., & Perinotto, M. 2000, A&A, 355, 713
Magrini, L., Vílchez, J. M., Mampaso, A., Corradi, R. L. M., & Leisy, P. 2007b, A&A, 470, 865
Maíz-Apellániz, J. 2004, PASP, 116, 859
Martin, D. C., Fanson, J., Schiminovich, D., et al. 2005, ApJ, 619, L1
Massey, P. & Hutchings, J. B. 1983, ApJ, 275, 578
Massey, P., McNeill, R. T., Olsen, K. A. G., et al. 2007, AJ, 134, 2474

Massey, P., Olsen, K. A. G., Hodge, P. W., et al. 2006, AJ, 131, 2478
Mayall, N. U. & Aller, L. H. 1942, ApJ, 95, 5
Meurer, G. R., Wong, O. I., Kim, J. H., et al. 2009, ApJ, 695, 765
Miller, W. W. I. & Cox, D. P. 1993, ApJ, 417, 579
Misselt, K. A., Clayton, G. C., & Gordon, K. D. 1999, ApJ, 515, 128
Morrissey, P., Schiminovich, D., Barlow, T. A., et al. 2005, ApJ, 619, L7
Oey, M. S. & Kennicutt, Jr., R. C. 1997, MNRAS, 291, 827
Oey, M. S. & Kennicutt, Jr., R. C. 1998, Publications of the Astronomical Society of Australia, 15, 141
Oke, J. B. 1990, AJ, 99, 1621
Palla, F. 2005, in IAU Symposium, Vol. 227, Massive Star Birth: A Crossroads of Astrophysics, ed. R. Cesaroni, M. Felli, E. Churchwell, & M. Walmsley, 196–205
Park, W.-K. & Lee, M. G. 2007, AJ, 134, 2168
Petersen, L. & Gammelgaard, P. 1997, A&A, 323, 697
Pflamm-Altenburg, J., Weidner, C., & Kroupa, P. 2009, MNRAS, 395, 394
Reach, W. T., Megeath, S. T., Cohen, M., et al. 2005, PASP, 117, 978
Reines, A. E., Johnson, K. E., & Hunt, L. K. 2008, AJ, 136, 1415
Relaño, M., Peimbert, M., & Beckman, J. 2002, ApJ, 564, 704
Reynolds, R. J., Roesler, F. L., & Scherb, F. 1974, ApJ, 192, L53+
Rosolowsky, E., Keto, E., Matsushita, S., & Willner, S. P. 2007, ApJ, 661, 830
Rosolowsky, E. & Simon, J. D. 2008, ApJ, 675, 1213
Roussel, H., Gil de Paz, A., Seibert, M., et al. 2005, ApJ, 632, 227
Salpeter, E. E. 1955, ApJ, 121, 161
Schlegel, D. J., Finkbeiner, D. P., & Davis, M. 1998, ApJ, 500, 525
Searle, L. 1971, ApJ, 168, 327
Thilker, D. A., Boissier, S., Bianchi, L., et al. 2007, ApJS, 173, 572
Thilker, D. A., Hoopes, C. G., Bianchi, L., et al. 2005, ApJ, 619, L67
Verley, S., Corbelli, E., Giovanardi, C., & Hunt, L. K. 2009, A&A, 493, 453
Verley, S., Corbelli, E., Giovanardi, C., & Hunt, L. K. 2010, A&A, 510, A64+
Verley, S., Hunt, L. K., Corbelli, E., & Giovanardi, C. 2007, A&A, 476, 1161
Viallefond, F., Goss, W. M., van der Hulst, J. M., & Crane, P. C. 1986, A&AS, 64, 237
Vilchez, J. M., Pagel, B. E. J., Diaz, A. I., Terlevich, E., & Edmunds, M. G. 1988, MNRAS, 235, 633
Voges, E. S., Oey, M. S., Walterbos, R. A. M., & Wilkinson, T. M. 2008, AJ, 135, 1291
Walterbos, R. A. M. & Braun, R. 1996, in Astronomical Society of the Pacific Conference Series, Vol. 106, The Minnesota Lectures on Extragalactic Neutral Hydrogen, ed. E. D. Skillman, 1–+
Weingartner, J. C. & Draine, B. T. 2001, ApJ, 548, 296
Wilson, C. D. & Scoville, N. 1990, ApJ, 363, 435
Wood, K. & Mathis, J. S. 2004, MNRAS, 353, 1126
Zepf, S. E., Ashman, K. M., English, J., Freeman, K. C., & Sharples, R. M. 1999, AJ, 118, 752